Retrieving frozen ground surface temperature under the snowpack in Arctic permafrost area from SMOS observations

Juliette Ortet[1, 2, 3], Arnaud Mialon[1], Alain Royer[3, 4], Mike Schwank[5, 6], Manu Holmberg[7], Kimmo Rautiainen[7], Simone Bircher-Adrot[8], Andreas Colliander[9], Yann Kerr[1], and Alexandre Roy[2, 3]

[1]Univ Toulouse, CNES/IRD/CNRS/INRAe, CESBIO, Toulouse, France
[2]Département des sciences de l'environnement, Université du Québec à Trois-Rivières, Trois-Rivières, Quebec, G9A 5H7, Canada
[3]Centre d'études nordiques, Québec, Quebec, G1V 0A6, Canada
[4]Département de géomatique appliquée, Université de Sherbrooke, Sherbrooke, J1K 2R1, Canada
[5]Swiss Federal Institute for Forest, Snow and Landscape Research WSL, Switzerland
[6]Gamma Remote Sensing Research and Consulting Ltd., Switzerland
[7]Finnish Meteorological Institute, Earth Observation Research Unit, Finland
[8]MétéoSuisse, Payerne, Switzerland
[9]NASA Jet Propulsion Laboratory, California Institute of Technology, Pasadena, CA, USA

Correspondence: Juliette Ortet (juliette.ortet@uqtr.ca)

Abstract. We developed and evaluated a new method to retrieve ground surface temperatures T_{g} below the snowpack from Soil Moisture and Ocean Salinity (SMOS) satellite L-band brightness temperatures (BT). The study was performed over 21 reference sites providing *in situ* ground temperatures $T_{\mathrm{g\text{-}insitu}}$ in Northern Alaska from 2011 to 2020, representative of Arctic tundra underlined by continuous permafrost, and with various open water fractions. T_{g} were obtained by inverting two types of microwave emission models (MEM) tailored for winter Arctic tundra environments. The first MEM assumed homogeneous SMOS pixels and optimized the surface roughness $H_{\mathrm{r,gs}}$. We observed the important influence of the frozen water bodies on T_{g} retrievals. Accordingly, we used a second more advanced MEM that accounts for the water surfaces within the SMOS pixels and describes their emission using an optimized water-ice interface roughness parameter, $H_{\mathrm{r,wi}}$. For sites with water fraction < 0.04, our methods (median R = 0.60) outperformed the European Centre for Medium-Range Weather Forecasts reanalysis (ERA5) product (median R = 0.51) with respect to the reference sites. The bias between retrieved and *in situ* temperature was slightly negative (median bias = -0.2°C). For sites with water fraction > 0.20, our water fraction correction reduced the bias, but the correlation of the T_{g} retrievals remained lower than that of ERA5. This study opens a new avenue for monitoring T_{g} below the snowpack in the Arctic using L-band BT, by inversion of a relatively simple MEM and limited auxiliary data. Extending this study to the whole Arctic area and taking advantage of the 15 years of SMOS data to study spatio-temporal variability of winter T_{g} in Arctic environments is excessively promising.

1 Introduction

The ground surface temperature T_{g} is a key parameter for physical land surface processes. The observed increase in the surface air temperatures over the last decades (Druckenmiller and Jeffries, 2019) and T_{g} (Biskaborn et al., 2019) in the Arctic regions

induced changes in land surface energy and water balance, impacting weather and climate at local and global scales (Schuur et al., 2015; Chadburn et al., 2017; Turetsky et al., 2020). A change in T_g affect surface runoff and hydrological processes (Rouse et al., 1997; Ala-Aho et al., 2021) and the ecosystem dynamics (Wang et al., 2019). In snow-covered conditions, T_g temporal dynamics are generally decoupled from air temperature (Bartlett et al., 2004; Cao et al., 2020) because of snow thermal insulation capacity (Zhang, 2005; Domine et al., 2019). Hence, T_g modulates the permafrost active layer dynamics and its spatial distribution (Dobiński, 2020). The Arctic freeze/thaw ground state associated with T_g is a key element of Arctic climate change feedbacks as T_g is the main driver of CO_2 release through soil respiration during winter (Natali et al., 2019; Mavrovic et al., 2023). However, meteorological stations over the Arctic are sparse and very few T_g observations are available due to harsh conditions (Shiklomanov, 2012). Model and reanalysis data provide T_g at a global scale for decades but in Arctic areas, the results remain uncertain (Royer et al., 2021b), mostly during winter when the Arctic is covered by snow (Herrington et al., 2024). Statistical, empirical, and machine learning models (Aalto et al., 2018; Lembrechts et al., 2022; Guo et al., 2024) were proposed but the insulation properties of snow coverage remain a major challenge to estimate T_g (Lembrechts et al., 2022).

Satellite remote sensing provides opportunities to map T_g in cold environments (Westermann et al., 2015). The land surface temperature (LST) can be retrieved based on thermal radiometry (e.g. Jiménez-Muñoz et al. (2014)). However, during winter, LST corresponds to the temperature of the snow surface (Westermann et al., 2012). High-frequency ($f > 10$ GHz passive microwave data (Fily, 2003; Jones et al., 2007; André et al., 2015) showed limited results for determining the T_g under the snowpack (Duan et al., 2020). Moreover, Köhn and Royer (2012) and Mialon et al. (2007) showed that when using Advanced Microwave Scanning Radiometer for EOS (AMSR-E) and Special Sensor Microwave/Imager (SSM/I) observations, the derived LST corresponds to a thin layer (skin) at the air-snow interface. Marchand et al. (2018) showed the potential of using passive microwaves to retrieve T_g by combining AMSR-E and Moderate-Resolution Imaging Spectroradiometer (MODIS) satellite data to inform a land surface scheme. However, the study was performed for a unique site and the integration of remote sensing data in a land surface scheme remains complex and operationally difficult to implement. It is well known that low microwave frequencies ($f < 10$ GHz) are less sensitive to snow properties, and L-band (protected frequency band $f = 1400$–1427 GHz, wavelength $\lambda \simeq 21$ cm) could provide unique information about the frozen ground under the snow (Schwank et al., 2015; Lemmetyinen et al., 2016; Roy et al., 2017).

In this study, we developed a new approach to retrieve T_g under the snowpack in tundra environments from Soil Moisture and Ocean Salinity (SMOS) observations. The emitted radiations observed by SMOS are expressed in terms of brightness temperature (BT), that are predominantly determined by the effective temperature and the emissivity of the observed scene. By considering that the Arctic ground surface remains frozen throughout winter, the ground emissivity remains constant and the BT depends mostly on T_g. However, even if the emissivity (driven by ground permittivity) remains constant, other contributions to the signal, including contributions from snow and water bodies, should be considered in retrieving T_g. We developed a microwave emission model (MEM) for Arctic tundra conditions to address the complex and heterogeneous scene observed at the SMOS footprint scale. The parameterization of central components such as the frozen ground permittivity, the snow layer, and the fraction of snow and ice covered water bodies and their impact on T_g retrievals were evaluated. The retrieved T_g

were validated against *in situ* measurements from 21 sites across northern Alaska and compared with the European Centre for Medium-Range Weather Forecasts (ECMWF) reanalysis (ERA5) ground temperatures $T_{\text{g-ERA5}}$ (Hersbach, H. et al., 2023). This satellite-based approach opens a new path towards soil temperatures monitoring under the snowpack in the Arctic with expected improvement in land and carbon cycle modeling in permafrost area.

2 Datasets

2.1 Brightness temperatures from SMOS

Operated by the European Space Agency (ESA), the SMOS satellite has been acquiring multi-angular BT at L-band since January 2010 (Kerr et al., 2010). We used the SMOS Level 3 brightness temperatures (L3BT) version 330 provided by the Centre Aval de Traitement des Données SMOS (CATDS) (CATDS, 2024). The L3BT are sampled on the global Equal Area Scalable Earth version 2.0 (EASE 2.0 grid, Brodzik et al. (2012)) using a cylindrical projection for daily ascending and descending orbits. Both vertical (V) and horizontal (H) polarizations are available for observation (off-nadir) angles θ from 0° to 60° binned over 5-degree intervals (Al Bitar et al., 2017). The SMOS measurements are impacted by Radio Frequency Interferences (RFI) (Daganzo-Eusebio et al., 2013), whose consequences vary in time, so morning and afternoon orbits were considered separately. The revisit time is shorter than the three-day revisit at the equator and enables observations of the study area at least once a day. The BT are associated with the estimated radiometric accuracy and sample standard deviation obtained in the averaging of measurements into observation angle bins.

2.2 *In situ* measurements of ground temperatures

The 21 reference in situ sites are located across Alaska (US), in the Arctic region (Figure 1 and Table 1). The continuous permafrost landscape integrates numerous lakes and some sites are located close to the coast (Barrow, Lake 145, Fish Creek, Camden Bay) while others are disseminated inland. All the selected sites are located above the tree line and are representative of the tundra environment with vegetation characterized by low shrubs and mosses (Table 1). SMOS observations are flagged for topography (Mialon et al., 2008), but none of the 21 in situ sites are impacted, except for the Atigun pass site which is labeled as moderate topography, i.e. SMOS data quality may be impacted by topography. The study sites are part of four different networks. The United States Geological Survey (USGS) (Urban, 2017) provided 14 sites from 1998 to 2019 as part of the Global Terrestrial Network for Permafrost (GTN-P). Three other sites come from the Carbon in Arctic Reservoirs Vulnerability Experiment (CARVE) (Oechel et al., 2016) between 2011 and 2015. The last four sites are part of the Soil Climate Analysis Network (SCAN) (Schaefer et al., 2007) and Snowpack Telemetry (SNOTEL) (Leavesley et al., 2010) and were accessed thanks to the International Soil Moisture Network (ISMN) (Dorigo et al., 2021). The *in situ* data is available with an hourly temporal resolution and was selected from January 2011 to coincide with SMOS observations. For each site, ground temperatures ($T_{\text{g-insitu}}$) at variable probing depth are available (Table 1). Other variables such as air temperature at 2 m height and snow depth are available.

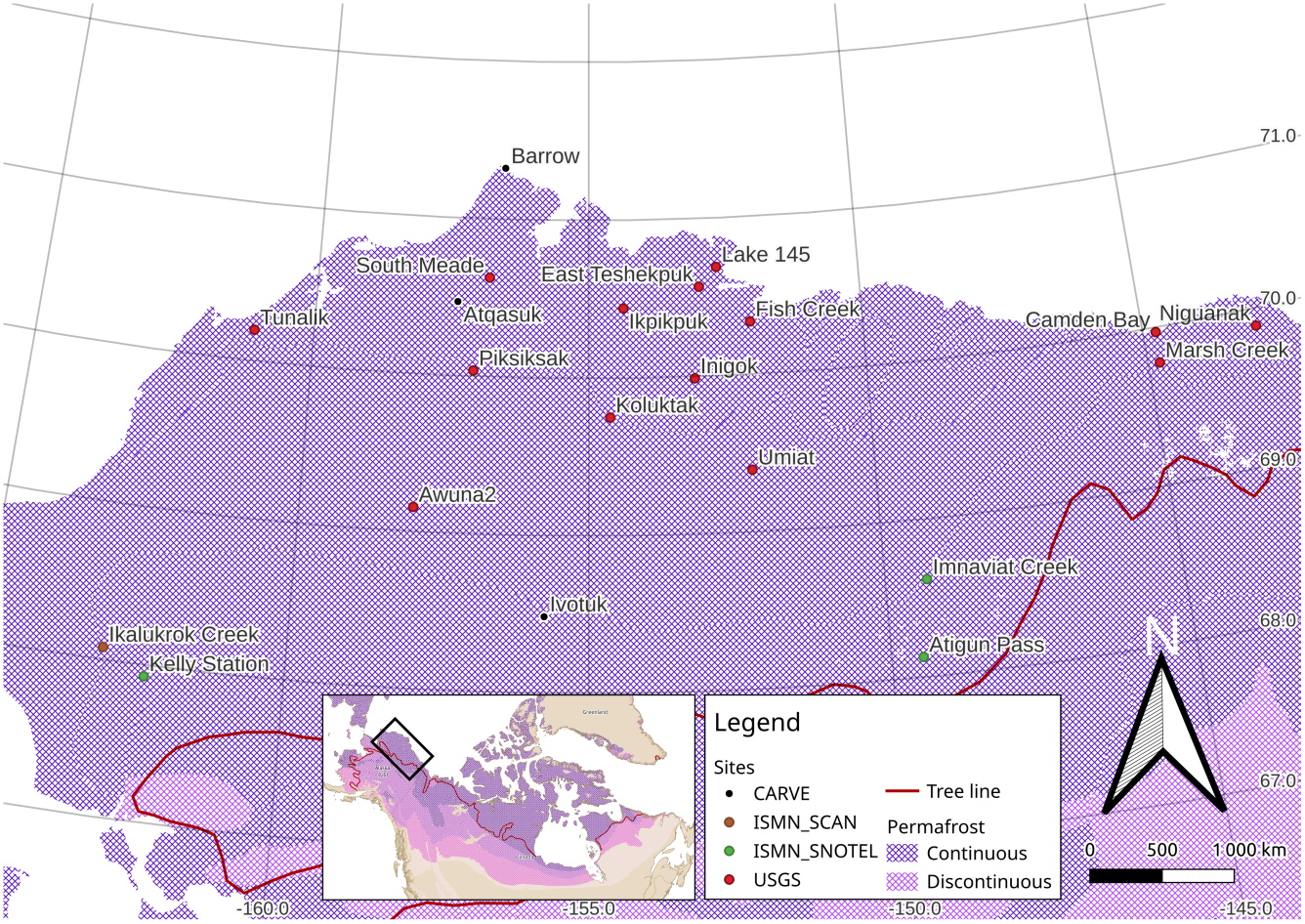

Figure 1. Distribution of the 21 ground-based $T_{\text{g-insitu}}$ stations used as a reference (background: the permafrost extent and tree line from Heginbottom et al. (2002). Sites coordinates are specified in Table 1.

2.3 Model reanalysis ground temperatures

The T_{g} retrieved from the L3BT was compared to the fifth generation ECMWF re-analysis (ERA5) ground temperature product (Hersbach, H. et al., 2023). We used the shallower soil temperature (Level 1, 0 - 7 cm depth) $T_{\text{g-ERA5}}$ provided on a 0.25° resolution grid with an hourly temporal resolution.

2.4 Land cover

The land cover fraction was calculated from the ESA CCI L4 map at a 300 m spatial resolution, Version 2.0.7 (2015) (Defourny, P. et al., 2023). To obtain the fraction of a given land cover class for one grid cell, the number of ESA CCI pixels of the corresponding class was divided by the total number of ESA CCI pixels in a round buffer around the grid cell center. A 40 km

Table 1. *In situ* stations coordinates with the associated available probe depths. The land cover fractions extracted from the ESA CCI L4 map at 300 m, Version 2.0.7 (2015) (ESA) using a 40 km diameter buffer around the closest SMOS L3 grid cell center for each study site. Only classes with fractions above 5% for at least one site are presented.

Network	Site	Latitude in °	Longitude in °	Probe depth(s) in cm	Sh.[1]	Gr.[2]	Li.Mo.[3]	S.v.(15) [4]	Fl. [5]	B.a.[6]	W.[7]
CARVE Oechel et al. (2016)	Atqasuk	70.47	-157.409	5	0.00	0.00	0.38	0.04	0.26	0.03	0.24
	Barrow	71.323	-156.597	5	0.00	0.01	0.40	0.13	0.14	0.00	0.32
	Ivotuk	68.486	-155.748	5	0.01	0.31	0.19	0.42	0.00	0.05	0.00
USGS Urban (2017)	Inigok	69.98962	-153.09384	5 to 120 †	0.00	0.00	0.57	0.16	0.00	0.00	0.23
	Fish Creek	70.33523	-152.052	5 to 120 †	0.00	0.00	0.30	0.04	0.06	0.00	0.59
	Umiat	69.39568	-152.14273	5 to 120 †	0.10	0.33	0.15	0.37	0.00	0.02	0.02
	Tunalik	70.19593	-161.07812	5 to 120 †	0.02	0.27	0.33	0.32	0.02	0.01	0.02
	Koluktak	69.7516	-154.61744	5 to 120 †	0.00	0.00	0.59	0.09	0.04	0.03	0.20
	Niguanak	69.88944	-142.9845	5 to 120 †	0.00	0.01	0.22	0.50	0.04	0.01	0.22
	Marsh Creek	69.77762	-144.79325	5 to 120 †	0.02	0.03	0.10	0.35	0.00	0.00	0.44
	South Meade	70.62847	-156.83532	5 to 120 †	0.00	0.00	0.39	0.04	0.24	0.02	0.27
	Camden Bay	69.97196	-144.77057	15	0.02	0.03	0.10	0.35	0.00	0.00	0.44
	Awuna2	69.156	-158.03005	15	0.03	0.74	0.02	0.19	0.00	0.00	0.00
	Piksiksak	70.03662	-157.08137	5 to 120 †	0.17	0.16	0.42	0.15	0.02	0.00	0.04
	East Teshekpuk	70.56852	-152.96498	5 to 120 †	0.00	0.00	0.38	0.05	0.15	0.01	0.41
	Ikpikpuk	70.44165	-154.36563	5 to 120 †	0.00	0.00	0.45	0.11	0.08	0.03	0.32
	Lake 145	70.6898	-152.63325	15	0.00	0.00	0.42	0.05	0.13	0.01	0.39
ISMN SNOTEL Leavesley et al. (2010)	Imnaviat Creek	68.62	-149.3	5 and 20	0.01	0.24	0.02	0.71	0.00	0.01	0.01
	Kelly Station	67.93	-162.28	5 and 20	0.42	0.15	0.09	0.09	0.00	0.06	0.03
	Atigun Pass	68.13	-149.48	5 and 20	0.02	0.03	0.34	0.33	0.00	0.24	0.01
ISMN SCAN Schaefer et al. (2007)	Ikalukrok Creek	68.08	-163.0	5 and 20	0.10	0.25	0.09	0.42	0.00	0.11	0.00

† "5 to 120" refers to all the available depths for the USGS sites, i.e. 5 – 10 – 15 – 20 – 25 – 30 – 45 – 70 – 95 – 120 cm.

[1] Shrubland [2] Grassland [3] Lichens and mosses [4] Sparse vegetation (tree shrub herbaceous cover) (<15%)

[5] Shrub or herbaceous cover flooded fresh/saline/barkish water [6] Bare areas [7] Water bodies

diameter buffer zone around each SMOS L3 grid cell center roughly corresponds to a 3 dB antenna pattern cut-off assimilated to the instrumental spatial resolution. The water fraction at each site was within a 40 km buffer. The land cover classes were used for the *in situ* environment characterization and the analysis of the results. The land cover fractions are summed up in Table 1. None of the sites are significantly covered by trees or high vegetation.

3 Methods

3.1 Pre-processing

Our retrievals were based on L-band T_{B} in H and V polarizations and at angles from 0 to 60°. The T_{B} were filtered if the RFI ratio (defined as the sum of the RFI flagged instances divided by the sum of the SMOS L1 views combined in each of the L3BT 5-degree angle bin) was more than 0.1. Due to the RFI situation in North America (Aksoy and Johnson, 2013), observations before 2012 were discarded. In winter, T_{g} under the snowpack is expected to be diurnally relatively stable (Bartlett et al., 2004). Consequently, we only focused on the daily morning (ascending) orbit passes (approx. 6 a.m local overpass). We used the $T_{\mathrm{g\text{-}insitu}}$ at 5 cm depth to focus on the same ground surface layer for all sites. An exception was made for Awuna2, Camden Bay, and Lake 145 where only 15 cm depth measurements were available. For each L3BT, we selected the closest $T_{\mathrm{g\text{-}insitu}}$ observed within 30 minutes of the mean satellite overpass time. The retrieval was performed only when $T_{\mathrm{g\text{-}insitu}} < -5$°C to ensure that ground conditions satisfy our stable frozen ground permittivity hypothesis (Pardo Lara et al., 2020). We also compared $T_{\mathrm{g\text{-}ERA5}}$ with respect to $T_{\mathrm{g\text{-}insitu}}$. For each site, we considered the nearest neighbor ERA5 node and used the closest time to the satellite overpass time.

3.2 Microwave emission model for the Arctic tundra during winter

Our proposed approach for T_{g} retrieval required an inversion model based on a MEM (Figure 2). The upwelling surface $T^{p}_{\mathrm{B,surf}}(\theta)$ was considered to be the linear combination of the upwelling BT from the snow-covered ground $T^{p}_{\mathrm{B,G}}(\theta)$, from the snow and ice covered water bodies $T^{p}_{\mathrm{B,WI}}(\theta)$ weighted by the water bodies fraction ν_{wi}:

$$T^{p}_{\mathrm{B,surf}}(\theta) = (1-\nu_{\mathrm{wi}}) \cdot T^{p}_{\mathrm{B,G}}(\theta) + \nu_{\mathrm{wi}} \cdot T^{p}_{\mathrm{B,WI}}(\theta) \tag{1}$$

$T^{p}_{\mathrm{B,G}}(\theta)$ and $T^{p}_{\mathrm{B,WI}}(\theta)$ were simulated with multi-layer configurations of the Two-Stream model (Schwank et al., 2014) and the Microwave Emission Model of Layered Snowpacks (MEMLS) (Mätzler and Wiesmann, 2012) reflecting the two emission model scenarios depicted in Figure 2. $T^{p}_{\mathrm{B,G}}(\theta)$ resulted from a submodel considering the snow and the atmosphere as two horizontal layers atop the ground which is an infinite half-space. Note that the low vegetation of the tundra is not considered in the submodel. In the case of $T^{p}_{\mathrm{B,WI}}(\theta)$, the submodel is made of three horizontal layers (ice, snow, and atmosphere) above the water as an infinite half-space. The layers and infinite half-spaces parametrizations are described in the following Sections (Sections 3.2.1, 3.2.2, 3.2.3). $T^{p}_{\mathrm{B,G}}(\theta)$ and $T^{p}_{\mathrm{B,WI}}(\theta)$ were also corrected from the atmosphere opacity $\tau_{\mathrm{atm}}(\theta)$. The deep sky and atmosphere upwelling and downwelling contributions were taken into account as in (Kerr et al., 2020), depending on

$T_{\mathrm{B,sky}}$, $T_{\mathrm{B,atm}}(\theta)$ and $\tau_{\mathrm{atm}}(\theta)$ (Table 2).

Our MEM considered microwave interactions at the interface between two layers: the reflectivity and the refractivity. The reflectivities of the smooth surface between layer n and $n+1$ are noted as $s^{\mathrm{H}*}(\theta)$ and $s^{\mathrm{V}*}(\theta)$ and were given by the Fresnel reflection coefficients (Ulaby and Long, 2014):

$$s^{\mathrm{H}*}(\theta) = \left| \frac{\sqrt{\varepsilon_n} \cdot A - \sqrt{\varepsilon_{n+1}} \cdot B}{\sqrt{\varepsilon_n} \cdot A + \sqrt{\varepsilon_{n+1}} \cdot B} \right|^2 \qquad s^{\mathrm{V}*}(\theta) = \left| \frac{\sqrt{\varepsilon_{n+1}} \cdot A - \sqrt{\varepsilon_n} \cdot B}{\sqrt{\varepsilon_{n+1}} \cdot A + \sqrt{\varepsilon_n} \cdot B} \right|^2 \tag{2}$$

$$\text{with} \quad A = \cos(\theta_n) \quad \text{and} \quad B = \sqrt{1 - (1 - A^2) \cdot \frac{\varepsilon_n}{\varepsilon_{n+1}}}$$

where H and V stand for horizontal and vertical polarization, θ account for the incidence angle and ε_n is the layer n complex dielectric constant.

The H-Q-N model (Wang and Choudhury, 1981) was proposed to empirically consider surface effects (including roughness) in the reflectivity and can be expressed as:

$$s^p(\theta) = [(1 - Q_{\mathrm{r}}) s_n^{p*}(\theta) + Q_{\mathrm{r}} s^{q*}(\theta)] \cdot \exp\left(-H_{\mathrm{r}} \cos^{N_{\mathrm{r}}^p}(\theta)\right) \tag{3}$$

where p and q are the two polarizations (q is H (resp. V) when p is V (resp. H)). The surface effects were taken into account with four parameters: the polarization mixing ratio Q_{r}, the angular effect parameters $N_{\mathrm{r}}^{\mathrm{H}}$, and $N_{\mathrm{r}}^{\mathrm{V}}$ and the effective roughness parameter H_{r}. These four parameters account for not only the geometric roughness effects but also the spatial heterogeneity of the surface characteristics. For instance, Escorihuela et al. (2007) showed a H_{r} dependence on soil moisture content for a ground-air interface. Our values for those parameters are detailed in the following sections and summed up in Table 2.

The angle deviation due to refractivity at the interface between the layers n and $n+1$ is given by Snell-Descartes law:

$$\theta_n = \arcsin\left(\sqrt{\frac{\varepsilon_{n+1}}{\varepsilon_n}} \sin\theta_{n+1}\right) \tag{4}$$

where ε_n is the layer n complex dielectric constant Ulaby et al. (1984).

3.2.1 Frozen ground parametrization

The bottom-most infinite half-space representing the ground was described using the following parameters: T_{g}, $\varepsilon_{\mathrm{frozen}}$, $H_{\mathrm{r,gs}}$, $Q_{\mathrm{r,gs}}$, $N_{\mathrm{r,gs}}^p$ (see Figure 2). The ground-snow interface reflectivity s_{gs}^p was obtained from equations 2 and 3. This study aimed to retrieve the ground surface temperature T_{g} by considering a fixed and constant ground permittivity in frozen conditions. Various models describe the ground permittivity at 1.4 GHz (Mironov et al., 2009; Bircher et al., 2016; Park et al., 2017), but very few in the case of frozen ground (Hallikainen et al., 1985; Mironov et al., 2015). The permittivity of a frozen ground was set to $\varepsilon_{\mathrm{frozen}} = 5.0 + 0.5$ i, similar to past studies (Schwank et al., 2014; Holmberg et al., 2024) and SMOS algorithm (Kerr et al., 2020). We considered the ground surface reflectivity as in Equation 3 accounting for various effects including roughness

using four parameters ($H_{\mathrm{r,gs}}$, $Q_{\mathrm{r,gs}}$, $N^{\mathrm{H}}_{\mathrm{r,gs}}$ and $N^{\mathrm{V}}_{\mathrm{r,gs}}$). The polarization mixing ratio $Q_{\mathrm{r,gs}}$ (Wang and Choudhury, 1981) as well as the angular effects parameters $N^{\mathrm{H}}_{\mathrm{r,gs}}$ and $N^{\mathrm{V}}_{\mathrm{r,gs}}$) were set to 0, as suggested by several studies (Kerr et al., 2020; Wigneron et al., 2011; Lawrence et al., 2013). $H_{\mathrm{r,gs}}$ value was optimized for all the sites using a range of 0 to 1 with 0.1 increments.

3.2.2 Dry snow parametrization

The layer accounting for the snow was defined by its effective temperature T_{s}, its permittivity ε_{s}, and the layer internal transmissivity t_{s} and reflectivity r_{s} (Figure 2). According to Schwank et al. (2015) and Rautiainen et al. (2016), dry snow is considered transparent at L-band, i.e. its internal transmissivity and reflectivity are $t_{\mathrm{s}} = 1$ (no absorption) and $r_{\mathrm{s}} = 0$ (no volume scattering). Consequently, our model became independent of T_{s}. However, Schwank et al. (2015) showed that air-snow interface impacts on impedance matching can not be ignored, i.e. the snow surface reflectivity $s^{p*}_{\mathrm{s}} \neq 0$. We considered refraction (Equation 4) and reflection for a smooth air-snow interface (Equation 2). The dry snow permittivity was set to $\varepsilon_{\mathrm{s}} = 1.53$ according to Equation 4 of Schwank et al. (2015) for a mean snow density $\rho_{\mathrm{s}} = 300$ kg m^3, which corresponds to the high Arctic snowpack average density observed by Derksen et al. (2014) and Roy et al. (2017). We assume a snowpack with the same parameters above the ground and the ice-covered water bodies.

3.2.3 Snow and ice covered water bodies parametrization

During winter, water bodies are fully covered by an ice layer with liquid water remaining below the ice layer (Adams and Lasenby, 1985; Jeffries et al., 2013). The ice layer was defined by its permittivity ε_{i} = 3.18 (Mätzler, 2006) and considered transparent (internal transmissivity $t_i = 1$ and internal reflectivity $r_i = 0$). However, smooth surface refraction (Equation 4) and reflection s^{p*}_{is} (Equation 2) were taken into account at the ice-snow interface. Similarly to the ground layer, the liquid water layer was defined with T_{w}, ε_{w}, $H_{\mathrm{r,wi}}$, $Q_{\mathrm{r,wi}}$ and $N^{p}_{\mathrm{r,wi}}$ (Figure 2). The water temperature T_{w} was considered constant throughout winter and equal to 2°C (Oveisy et al., 2012). We consider fresh water whose L-band permittivity ε_{w} was fixed to $86 + 13$ i (Liebe et al., 1991; Mätzler, 2006; Ulaby and Long, 2014). The water-ice interface reflectivity s^{p}_{wi} was obtained from equation 3, accounting for the water-ice interface heterogeneity. $Q_{\mathrm{r,wi}}$, $N^{\mathrm{H}}_{\mathrm{r,wi}}$ and $N^{\mathrm{V}}_{\mathrm{r,wi}}$ were set to 0 (Choudhury et al., 1979). $H_{\mathrm{r,wi}}$ value was optimized for all the sites on a range of 0 to 2 with an iteration step of 0.1. The water body ν_{wi} accounted for the area percentage of the considered SMOS node covered by water bodies based on the water class from ESA CCI landcover (Table 1).

3.2.4 Microwave emission model configurations

Figure 2 depicts a schematic of the MEMs and Table 2 summarizes the input parameters. This study tested two configurations: one considering a homogeneous scene with only ground (hereafter named MEM$_{\mathrm{G}}$) and one with a heterogeneous scene composed of ground and snow and ice covered water bodies (hereafter named MEM$_{\mathrm{G+WI}}$).

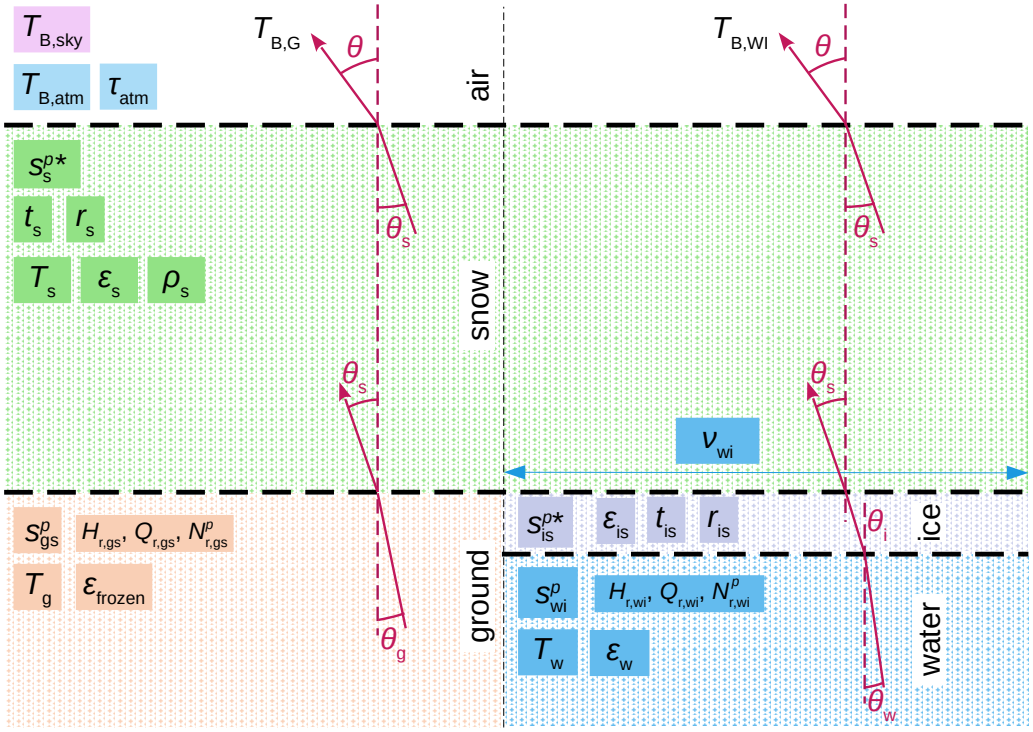

Figure 2. Schematic representation of the MEMs for modeling a winter tundra scene at L-band. $\mathrm{MEM_G}$ only considers the left side of the sketch, $\mathrm{MEM_{G+WI}}$ considers both sides.

Table 2. Input parameters values of the MEM for modeling a winter tundra scene at L-band.

Layer	Parameter	Description	Value
Atmosphere	$T_{\mathrm{B,sky}}$	Deep sky BT	2.7 K
	$T_{\mathrm{B,atm}}$	Atmosphere BT	2.2 K at nadir†
	τ_{atm}	Atmosphere opacity	0.01 at nadir†
Snow	s_{s}^{p*}	Snow-air interface reflectivity	Equation 2
	t_{s}	Snow internal transmissivity	1
	r_{s}	Snow internal reflectivity	0
	ε_{s}	Dry snow permittivity	1.53
	ρ_{s}	Mean snow density	300 kg m^{-3}
Ground	s_{gs}^{p}	Ground-snow reflectivity	Equation 3
	$H_{\mathrm{r,gs}}$	Ground roughness	[0-1]
	$Q_{\mathrm{r,gs}}$	Ground polarization ratio	0
	$N_{\mathrm{r,gs}}^{\mathrm{H}}$	Ground angular dependent effects (in H)	0
	$N_{\mathrm{r,gs}}^{\mathrm{V}}$	Ground angular dependent effects (in V)	0
	$\varepsilon_{\mathrm{frozen}}$	Frozen ground permittivity	$5 + 0.5$ i
	T_{g}	Effective ground temperature	Retrieved
Water body	ν_{wi}	Water body fraction	0 or Table 1
	s_{is}^{p*}	Ice-snow reflectivity	Equation 2
	r_{i}	Ice internal reflectivity	0
	t_{i}	Ice internal transmissivity	1
	ε_{i}	Ice permittivity	3.18
	s_{wi}^{p}	Water body-ice reflectivity	Equation 3
	$H_{\mathrm{r,wi}}$	Water body roughness	[0-1]
	$Q_{\mathrm{r,wi}}$	Water body polarization ratio	0
	$N_{\mathrm{r,wi}}^{\mathrm{H}}$	Water body angular dependent effects (in H)	0
	$N_{\mathrm{r,wi}}^{\mathrm{V}}$	Water body angular dependent effects (in V)	0
	ε_{w}	Water permittivity	$86 + 13$ i
	T_{w}	Water temperature	2°C

† Example value for $\theta = 0°$. For all the angles, $T_{\mathrm{B,atm}}$ and τ_{atm} are calculated as in Kerr et al. (2020).

3.3 Cost function for frozen ground temperature retrievals

Both $\mathrm{MEM_G}$ and $\mathrm{MEM_{G+WI}}$ described in Section 3.2 were inverted to retrieve the frozen ground temperature T_g, by minimizing the following cost function:

$$\mathrm{CF}(T_\mathrm{g}) = \sum_{p,\theta_k} \left(\frac{T^p_{\mathrm{B,obs}}(\theta_k) - T^p_{\mathrm{B,sim}}(\theta_k, T_\mathrm{g})}{\sigma T^p_\mathrm{B}(\theta_k)} \right)^2 \quad (5)$$

where $T^p_{\mathrm{B,obs}}(\theta_k)$ and $T^p_{\mathrm{B,sim}}(\theta_k, T_\mathrm{g})$ are the observed and simulated BT for both H and V polarizations and at various incidence angle bins θ_k. The BT standard deviation $\sigma T^p_\mathrm{B}(\theta_k)$ is computed from the estimated radiometric accuracy and sample standard deviation obtained in the averaging of measurements into observation angle bin k.

3.4 Post-processing

The first aim of the post-processing was to reduce the influence of outliers. The retrieved T_g below the first 1% quantile and above the last 99% quantile of each site were considered outliers and discarded. We removed the $T_{\mathrm{g\text{-}ERA5}}$ at these dates in the ERA5 time series to ensure that we compared a data pull with the same size. A low short-term variability is expected between T_g under the snowpack that acts like a thermal insulator. The final step smoothed the T_g time series to reduce the impact of the noise in SMOS BT to the retrievals. We used a z-score smoothing, to limit the variations of T_g to 1 standard deviation for a 5-day window. At a date t, the local average $\overline{T^t_\mathrm{g}}$ and standard deviation $\sigma\left(T^t_\mathrm{g}\right)$ are calculated for a 5-day window around each T^t_g. If $T^t_\mathrm{g} > \overline{T^t_\mathrm{g}} + 1 \cdot \sigma\left(T^t_\mathrm{g}\right)$, T^t_g is replaced by $\overline{T^t_\mathrm{g}}$.

3.5 Metrics

Three statistical indicators were used to assess the comparison between the retrieved T_g and the reference temperatures $T_{\mathrm{g\text{-}insitu}}$ ((Entekhabi et al., 2010; Gruber et al., 2020)). The unbiased Root Mean Square Deviation (ubRMSD) is used for uncertainty estimation as it is corrected from the bias between the two time series (Kerr et al., 2016a; Benninga et al., 2020). The bias corresponds to the mean difference between the compared time series of T_g and $T_{\mathrm{g\text{-}insitu}}$. The Pearson correlation coefficient (R) accounts for the similarities in temporal dynamics of the two time series. Each metric was computed for the whole time series for each site. Each metric was computed for the whole time series for each site and was provided with its confidence intervals (CI) at 5 and 95%. Analytical solutions enabled us to find the CI of the bias, the ubRMSD and the R (Gruber et al., 2020). We also evaluated $T_{\mathrm{g\text{-}ERA5}}$ with respect to $T_{\mathrm{g\text{-}insitu}}$ with similar metrics.

4 Results

The metrics (bias, R and ubRMSD) for all sites and obtained with both $\mathrm{MEM_G}$ and $\mathrm{MEM_{G+WI}}$ are summarized in Appendix D. This results section first focuses on the $H_{\mathrm{r,gs}}$ and $H_{\mathrm{r,wi}}$ optimization based on the biases (Section 4.1) and then evaluates the T_g retrievals (Section 4.2).

4.1 Parameters optimization evaluation

4.1.1 $H_{\mathrm{r,gs}}$ optimization

In the $\mathrm{MEM_G}$ configuration, we retrieved T_{g} by testing $H_{\mathrm{r,gs}}$ values from 0 to 1 with 0.1 increments. Figure 3 shows the biases obtained with all tested $H_{\mathrm{r,gs}}$ and biases obtained with $T_{\mathrm{g\text{-}ERA5}}$ for each site, with respect to $T_{\mathrm{g\text{-}insitu}}$. For all sites, the bias changed in the negative direction with increasing $H_{\mathrm{r,gs}}$. For sites with $\nu_{\mathrm{wi}} \leq 0.04$, the biases went from positive down to negative values with increasing $H_{\mathrm{r,gs}}$, except for Awuna2 and Umiat whose biases remained positive. For sites with $\nu_{\mathrm{wi}} \geq 0.20$, the biases of numerous sites remained negative and went down close to -30°C. This suggests that the water bodies strongly impact the T_{g} retrieval bias. That is why we optimized the value of $H_{\mathrm{r,gs}}$ only on sites less affected by water bodies. For sites with $\nu_{\mathrm{wi}} \leq 0.04$, the bias was minimized with $H_{\mathrm{r,gs}}$ = 0.8 (average = 0.2°C, median = -0.2°C, Q1 = -1.6°C, Q3 = 0.8°C, range = 2.4°C). Surprisingly, the sites with the highest ν_{wi} (between 0.44 and 0.59) showed positive biases for some $H_{\mathrm{r,g}}$.

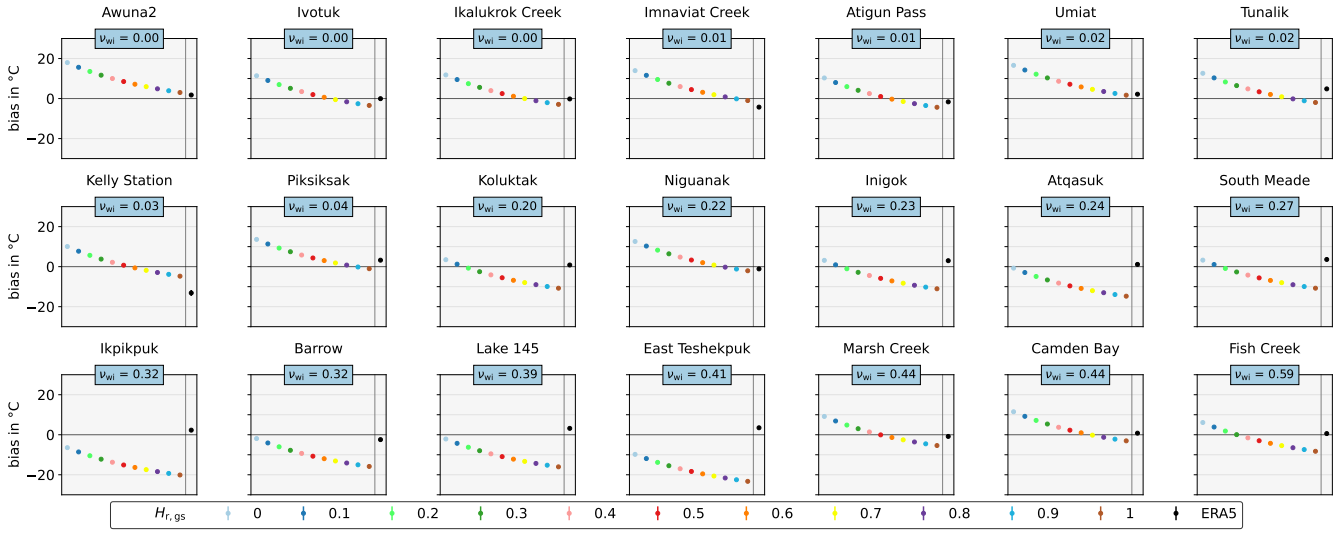

Figure 3. Bias per site for each $H_{\mathrm{r,gs}}$ used in the inversion with the $\mathrm{MEM_G}$ model. Each graph corresponds to one site. $H_{\mathrm{r,gs}}$ values are represented by a unique color and are ranged from 0 to 1 on the x-axis. The last point of each graph, in black, is obtained with $T_{\mathrm{g\text{-}ERA5}}$. The y-axis corresponds to the bias $T_{\mathrm{g}} - T_{\mathrm{g\text{-}insitu}}$. Each point is symbolized with error bars that correspond to the confidence interval. The sites are ordered in ascending order of water fraction (ν_{wi} in the light blue box).

4.1.2 $H_{\mathrm{r,wi}}$ optimization

The results in Section 4.1.1 showed that the T_{g} retrieval bias strongly depends on water fraction. The $\mathrm{MEM_{G+WI}}$ model accounted for the presence of frozen water bodies (i.e. $\nu_{\mathrm{wi}} \neq 0$) in the T_{B} calculation (Figure 2). In this configuration, T_{g} was retrieved with different tested $H_{\mathrm{r,wi}}$ values from 0 to 1 with 0.1 increments. $H_{\mathrm{r,gs}}$ was set to 0.8 as shown in Section 4.1.1. For each site, Figure 4 shows the biases obtained with various $H_{\mathrm{r,wi}}$ and compared with $T_{\mathrm{g\text{-}ERA5}}$ bias with respect to $T_{\mathrm{g\text{-}insitu}}$. The

higher $H_{\mathrm{r,wi}}$ the more negative the bias, while slope of the variations is linked to ν_{wi}. As expected, for sites with $\nu_{\mathrm{wi}} \leq 0.04$, the biases showed little variations for all $H_{\mathrm{r,wi}}$. At Piksiksak ($\nu_{\mathrm{wi}} = 0.04$) bias went from 5.2°C ($H_{\mathrm{r,wi}} = 0$) down to 2.0°C $H_{\mathrm{r,wi}} = 1$. For sites with $\nu_{\mathrm{wi}} \geq 0.20$, the biases highly varied with increasing $H_{\mathrm{r,wi}}$. For instance at Atqasuk ($\nu_{\mathrm{wi}} = 0.24$), the bias decreased from 16.5°C to -7.8°C with $H_{\mathrm{r,wi}} = 0$ and $H_{\mathrm{r,wi}} = 1$. At East Teshekpuk ($\nu_{\mathrm{wi}} = 0.41$), the bias for the $H_{\mathrm{r,wi}}$ extrema decreased from 37.0°C to -16.7°C. For the sites with the highest ν_{wi} (between 0.44 and 0.59), all the biases remained larger than 15°C for the tested $H_{\mathrm{r,wi}}$ range. Consequently, we do not consider them in the following analysis of the water body correction method. For the sites with $0.20 \leq \nu_{\mathrm{wi}} \leq 0.41$, the bias was minimized with $H_{\mathrm{r,wi}}$ = 0.7 (average = 0.7°C, median = 0.2°C, Q1 = -2.9°C, Q3 = 2.8°C, range = 5.7°C).

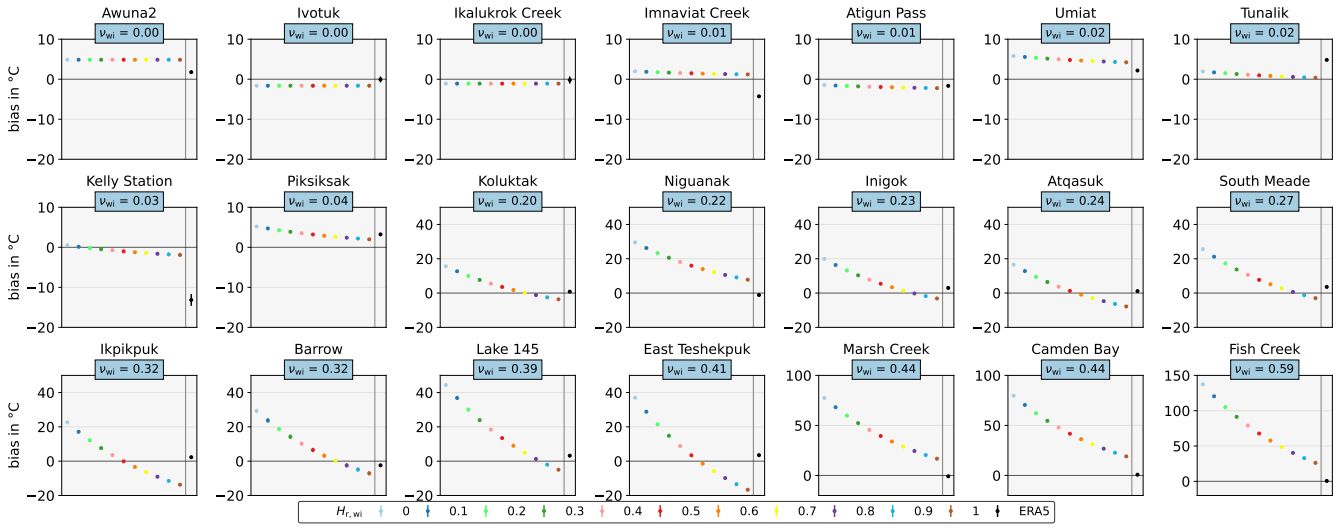

Figure 4. Bias per site for each $H_{\mathrm{r,wi}}$ used in the inversion. Each graph corresponds to one site. $H_{\mathrm{r,wi}}$ values are represented by a unique color and marker combination (see Legend) and are ranged from 0 to 1 with a 0.1 step on the x-axis. The last point of each graph, in black, is obtained with $T_{\mathrm{g\text{-}ERA5}}$. The y-axis corresponds to the bias $T_{\mathrm{g}} - T_{\mathrm{g\text{-}insitu}}$. Note that the y-axis scale is variable. Each point is symbolized with error bars that correspond to the 5-95% confidence interval. The sites are ordered in ascending order of water fraction (ν_{wi} in the light blue box).

4.2 T_{g} retrievals evaluation

4.2.1 T_{g} retrievals for sites with $\nu_{\mathrm{wi}} \leq 0.04$

The R, bias, and ubRMSD using $\mathrm{MEM_G}$ with $H_{\mathrm{r,gs}}$ = 0.8 and $\mathrm{MEM_{G+WI}}$ with $H_{\mathrm{r,wi}}$ = 1 were compared to $T_{\mathrm{g\text{-}ERA5}}$ metrics in Figure 5. For the sites with $\nu_{\mathrm{wi}} \leq 0.04$, when accounting for the water bodies with $\mathrm{MEM_{G+WI}}$, we selected $H_{\mathrm{r,wi}}$ = 1 for the ice-water interface as it minimized the bias average of these sites (average = 0.6°C). Each metric (in grey) is given with its confidence limits at 5% (orange) and 95% (blue). This representation enables us to show the dispersion of the metrics for all the considered sites. The R values of the retrieved T_{g} (median = 0.60 for both $\mathrm{MEM_G}$ and $\mathrm{MEM_{G+WI}}$) were better than

ERA5 (median = 0.51). Moreover, in the case of ERA5, the interquartile range was larger (Q1 = 0.33, Q3 = 0.55, range = 0.22) and the 5% confidence limit went down negative values. All the biases are centered around zero (mean = 0.2°C for $\mathrm{MEM_G}$, 0.6°C for $\mathrm{MEM_{G+WI}}$ and -0.8°C for ERA5), and all the absolute biases were lower than 5°C, except an outlier for ERA5 with a strong negative bias = -13.1°C (Kelly Station, according to Figure 3). The ubRMSD from both inversions (median = 2.1°C for both $\mathrm{MEM_G}$ and $\mathrm{MEM_{G+WI}}$) were significantly smaller than the ones from ERA5 (median = 3.9°C).

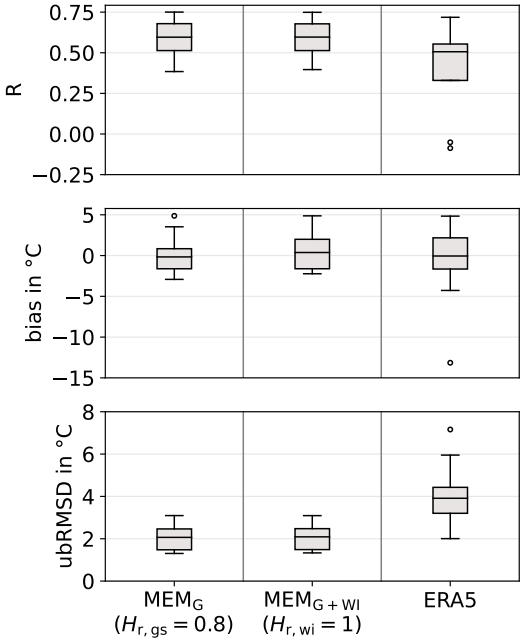

Figure 5. Summary statistics of R, bias and ubRMSD for sites with $\nu_{\mathrm{wi}} \leq 0.04$. The boxes show the median and interquartile range and whiskers show the 5 and 95 percentiles obtained from all the considered sites. The boxes correspond to the skill estimate (R, bias, or ubRMSD). The associated 5% and 95% CI are provided in Figure B1. The x-axis corresponds to the $H_{\mathrm{r,wi}}$ used in the inversion. The boxes are respectively obtained from: $\mathrm{MEM_G}$ with $H_{\mathrm{r,gs}}$ = 0.8 (left), $\mathrm{MEM_{G+WI}}$ with $H_{\mathrm{r,wi}}$ = 1 (center) and ERA5 (right).

4.2.2 T_g retrievals for sites with $0.20 \leq \nu_{wi} \leq 0.41$

The overall R, bias and ubRMSD for $\mathrm{MEM_{G+WI}}$ with different $H_{\mathrm{r,wi}}$ are summarized in Figure 6 with the corresponding $\mathrm{MEM_G}$ (with $H_{\mathrm{r,gs}}$ = 0.8) and ERA5 metrics. Similarly to Figure 5, the boxes show the metrics dispersion. The R values remained the same for all $H_{\mathrm{r,wi}}$ and equal to the R reached with $\mathrm{MEM_G}$ (median R = 0.21), but lower than ERA5 (median R = 0.62). The biases went more negative with increasing $H_{\mathrm{r,wi}}$ values. The bias was minimized for $H_{\mathrm{r,wi}}$ = 0.7 (Section 4.1.2), with a median value (0.2°C) which was closer to 0 than the bias with $\mathrm{MEM_G}$ (median = -13.0°C) and with ERA5 (median = 2.3°C). Yet, for bias, the interquartile range for $H_{\mathrm{r,wi}}$ = 0.7 (Q1 = -2.9°C, Q3 = 2.8°C, range = 5.7°C) remained much larger than ERA5 (Q1 = 0.8°C, Q3 = 3.2°C, range = 2.4°C), which meant that the bias remained higher for some of the sites. A wider

range (Q1 = 4.4°C, Q3 = 6.6°C, range = 2.2°C) was also observed for the ubRMSD for all the $H_{\mathrm{r,wi}}$ and $\mathrm{MEM_G}$ (Q1 = 3.7°C, Q3 = 5.3°C, range = 1.6°C) with respect to ERA5 (Q1 = 3.2°C, Q3 = 3.5°C, range = 0.2°C).

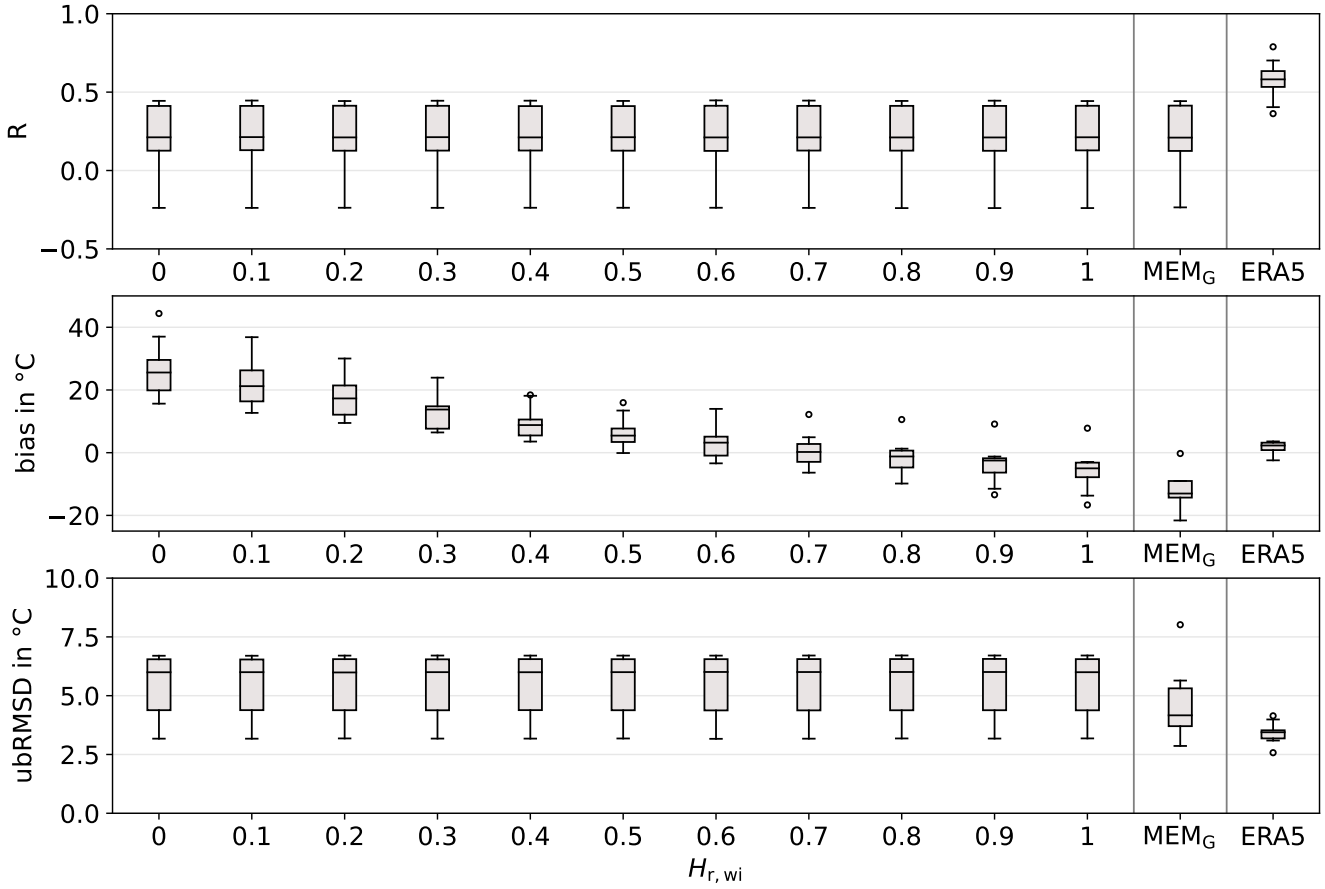

Figure 6. Summary statistics of R, bias and ubRMSD for sites with $0.20 \leq \nu_{\mathrm{wi}} \leq 0.41$. The associated 5% and 95% CI are provided in Figure B2. Boxes represent the site median and interquartile range (Q_3 - Q_1) and whiskers represent the 5 and 95 percentiles. The x-axis corresponds to the $H_{\mathrm{r,wi}}$ used in the inversion. The rightmost boxes are obtained with ERA5.

5 Discussion

The SMOS satellite was originally designed to focus on soil moisture and ocean salinity, but the applications extend to biomass monitoring (Kerr et al., 2010, 2016b; Mialon et al., 2020) and soil freeze-thaw state (Rautiainen et al., 2014, 2016). Recently, cryosphere applications have been increasingly investigated (Leduc-Leballeur et al., 2020; Schwank et al., 2021; Holmberg et al., 2024). The synergy between theses studies should be further explored. For instance, producing T_{g} maps over the Arctic could complement the information from the freeze-thaw state products. In addition, this satellite-based approach is a first attempt to monitor the soil temperatures under the snowpack in the whole circumarctic permafrost area. Based on L-band

observations of SMOS since 2010, continuing efforts in long-term and operational permafrost state monitoring would be made possible by the upcoming satellite missions CIMR and CryoRad (Donlon et al., 2023; Macelloni et al., 2018). Such soil temperature measurements would be highly beneficial for climate monitoring and carbon cycle modeling. Future work will look at integrating our approach to assimilation approaches such as the SMAPLv4 to improve soil temperature in winter and winter soil CO_2 emission.

The retrieval model parametrization evaluation showed clear contrasting results according to the water bodies' fraction over sites. T_{g} retrievals outperformed ERA-5 when $\nu_{\mathrm{wi}} \leq 0.04$ but are mitigated when $\nu_{\mathrm{wi}} \geq 0.20$. Improvement of the T_{g} retrievals may be further explored with more complex modeling, auxiliary data, or a 2-parameter inversion. Previous studies have shown the effects of ground permittivity and snow density to L-band BTs at theoretical, tower-based radiometer, and satellite scales, Schwank et al. (2014); Lemmetyinen et al. (2016); Roy et al. (2017); Holmberg et al. (2024). We can expect the same for snow density and ground temperature. So a joined retrieval of T_{g} and snow density may remove some artifacts due to the snow signal in the retrieved T_{g} time series. However, additional prior information may have to be needed to ensure inversion stability. In the high-latitude areas, the revisit time is short. For all the sites, the median value of the difference between $T_{\mathrm{g\text{-}insitu}}$ at days t and $t+1$ is 0.03°C. This difference remains at 0.1°C for a 3-day lag. Thus, $T_{\mathrm{g\text{-}insitu}}$ is very stable for short time range, which supports the thermal insulation of the snowpack. Considering a small temporal variation of T_{g} due to the snowpack thermal insulation, retrievals could be based on observations from multiple orbits (Konings et al., 2016). This could decrease the impact of the instrumental noise on the retrievals.

5.1 T_{g} retrievals under the snowpack for sites with $\nu_{\mathrm{wi}} \leq 0.04$

For sites with $\nu_{\mathrm{wi}} \leq 0.04$, correlation, bias and ubRMSD of the retrieval were superior to ERA5. A slightly negative bias was observed when the ν_{wi} was ignored (using the model $\mathrm{MEM_G}$) but was successfully corrected with a model that accounts for snow and ice covered water bodies $\mathrm{MEM_{G+WI}}$.

5.1.1 Frozen ground parametrization

We used a frozen ground permittivity of $\varepsilon_{\mathrm{frozen}} = 5 + 0.5\,\mathrm{i}$, as defined by Hallikainen et al. (1985) and which was commonly used in various studies (Schwank et al., 2014; Kerr et al., 2020; Holmberg et al., 2024). The emission depth of L-band observations is usually associated with the first 5 cm of the ground (Schmugge, 1983). However, the emission depth varies with the ground state and texture, based on the ground attenuation constant α ($\delta_{\mathrm{e}} = 1/2\alpha$ Ulaby and Long (2014)), and consequently the ground complex dielectric constant ε_{g}. For $\varepsilon_{\mathrm{frozen}} = 5.0 + 0.5\,\mathrm{i}$, the calculation based on Ulaby and Long (2014) shows that the associated emission depth $\delta_{\mathrm{e}} \simeq 15$ cm. When it comes to frozen ground, the effective depth is still not well defined and it becomes even more complex with a snow layer on top of the ground. Rautiainen et al. (2012) estimated the emission depth of frozen ground at a maximum of 50 cm, but observed a T_{B} saturation only when reaching a 30 cm frost depth. By computing metrics for $T_{\mathrm{g\text{-}insitu}}$ at all the available depths for the sites with $\nu_{\mathrm{wi}} \leq 0.04$, we found that R was better than ERA5 (median = 0.51) for depth down to 30 cm (median range from 0.57 to 0.74) (Figure 7). For *in situ* measurements down to 45 cm, the median absolute biases were smaller than 1.5°C and the median ubRMSD were smaller than 2.5°C. These results suggest that

the sensitivity depth is in fact down to 50 cm or less. For deeper $T_{\text{g-insitu}}$, the correlation decreased to negative values (median R = -0.18 for depth = 120 cm). Note that for the period of this study (focused on $T_{\text{g-insitu}}$ < -5°C at 5 cm depth) the ground was fully frozen down to 50 cm for the 11 USGS sites that provide ground temperatures down to 120 cm. Due to potential shallow frozen soil, emissions from the underlying unfrozen soil should be taken into account in the early winter (Rautiainen et al., 2012). As observed by Schwank et al. (2004), the observed signal can encompass a contribution of the boundary between frozen and unfrozen soil, which was not taken into account in our modeling.

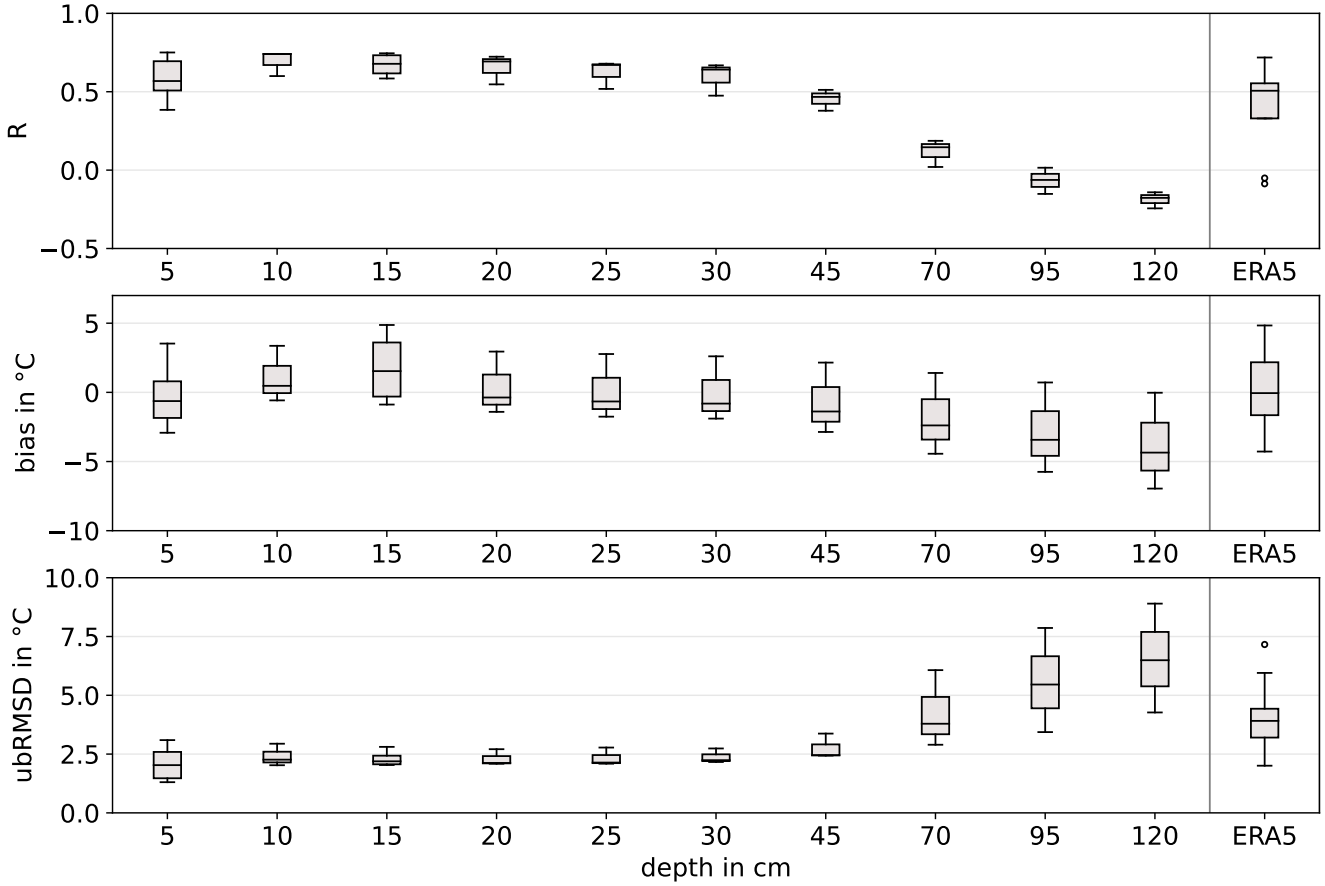

Figure 7. Summary statistics of R, bias and ubRMSD for sites with $\nu_{\text{wi}} \leq 0.04$. The associated 5% and 95% CI are provided in Figure 7. Boxes represent the site median and interquartile range (Q_3 - Q_1) and whiskers represent the 5 and 95 percentiles. The x-axis corresponds to the *in situ* probing depths used for the validation. The extreme right boxes are obtained with ERA5 and $T_{\text{g-insitu}}$ at 5 cm depth.

Concerning the ground surface parameters, the commonly used H-Q-N empirical model has been tuned for SM and VOD retrievals in many studies (Parrens et al., 2017; Chaubell et al., 2020; Preethi et al., 2024). Hence, its parametrization should be optimized for T_{g} retrievals in arctic environment. We found the optimized set of values $H_{\text{r,gs}} = 0.8, Q_{\text{r,gs}} = 0, N^{\text{H}}_{\text{r,gs}} = 0, = N^{\text{V}}_{\text{r,gs}} = 0$ for the snow-ground interface, which is consistent with Holmberg et al. (2024). This parametrization depends on the

chosen ground permittivity value. According to the Fresnel reflection coefficients (Equation 2), increasing ground permittivity leads to a decrease of the emissivity. Using the H-Q-N model (Equation 3), increasing $H_{\mathrm{r,gs}}$ means an increase of the emissivity. Thus, the soil parametrization requires a joint optimization of ε_{g} and $H_{\mathrm{r,gs}}$.

We optimized $H_{\mathrm{r,gs}}$ based on a permittivity of a frozen ground value of $\varepsilon_{\mathrm{frozen}} = 5 + 0.5$ i, but this value could be re-evaluated. The soil permittivity depends on the soil liquid water content and other characteristics (e.g. texture and bulk density). Based on a review of ground permittivity models (see Section 5.1.1), we investigated other potential values for frozen soil permittivity. For a frozen ground ($T_{\mathrm{g}} < -5$°C), we assumed the water to be completely frozen and thus SM negligible, i.e. $SM \simeq 0$ m^3 m^{-3} (Zhang et al., 2010; Mavrovic et al., 2023). Soil property information (clay fraction, sand fraction, soil organic content, and bulk density) was extracted at each site location from the SoilGrids 250 m v2.0 database (Poggio et al., 2021) for the 0–5 cm soil layer (Table A1 in the appendices). The Soil Organic Carbon (SOC) content was very high at all the sites, as expected in the Arctic region, i.e five to ten times higher than the global mean 40 g kg^{-1} (according to SoilGrid v2.0), and so was the bulk density. Dielectric constant models like the commonly used Mironov model do not use the SOC information to compute the permittivity. It was first designed considering SM and clay content (Mironov et al., 2009). It was then further developed to use SM, T_{sg} (here set as -20°C), and bulk density (Mironov et al., 2015). Park et al. (2017) was based on silt, clay, and sand contents, and bulk density. Bircher et al. (2016) defined a soil permittivity model tailored for high organic content soils, whereas Park's model was updated to consider soil organic content (Park et al., 2019). The permittivities computed with these models for our sites are summarized in Table A2 in the appendices. The obtained $\varepsilon_{\mathrm{frozen}}$ real parts went from 1 to 4, while the imaginary parts ranged from 0 to 0.1. This comparison of various permittivity models that depend on soil texture showed that the permittivity variability for frozen arctic soils was low and legitimate the use of a fixed value for the ground permittivity. However, the obtained permittivities were significantly lower than $\varepsilon_{\mathrm{frozen}} = 5.0 + 0.5$ i. This could be an evidence that $SM > 0$ m^3 m^{-3}, even in frozen ground conditions ($T_{\mathrm{g}} < -5$°C). In addition, a permittivity equal to $\varepsilon_{\mathrm{frozen}} = 5.0 + 0.5$ i may result from a soil surface which was saturated with water at freezing time. But, as the Arctic soil shows high SOC and high bulk density (Table A1), it may not satisfy this water saturation condition. For the imaginary part of the permittivity, Mironov et al. (2015) showed a decrease with decreasing temperatures. *In situ* measurements of frozen ground permittivity could be valuable, simultaneously to tower-based radiometer observations in the Arctic tundra environment. Some probes seem efficient for this task, such as the one described in Gélinas et al. (2025). Using a constant permittivity, calculated under the assumption of a homogeneous ground, is a practical solution for our model, as it reduces the number of free parameters and auxiliary data. However, dielectric mixing models enable to characterize heterogeneous materials (Ulaby and Long, 2014) and could better fit the Arctic soils local behaviour.

5.1.2 Effects of the snow layer

Snow cover was present for all ground temperature observations used in T_{g} retrievals (i.e., the observed snow depth was above 10 cm), motivating the use of a snow layer in the MEM model. Lemmetyinen et al. (2016) and Roy et al. (2017) suggested that snow emissions at L-band are related to the bottom 10 cm of the snow layer. The typical Arctic snow profile consists of a dense windslab of high density ($\rho \simeq 300 - 400$ kg m^{-3}) but with a depth hoar underneath with lower density ($\rho \simeq 250$ kg m^{-3}) (**?**).

However, the impact in terms of ε_s is low in the model of Wiesmann and Mätzler (1999) that we used in the present study ($\varepsilon_s(\rho = 300$ kg m$^{-3}) \simeq 1.5$ and $\varepsilon_s(\rho = 250$ kg m$^{-3}) \simeq 1.4$). In addition, our model does not account for the inclusion of ice crusts in the snowpack (e.g. after rain-on-snow (ROS) events) (Bartsch et al., 2023), nor low vegetation (e.g. shrubs or mosses) that could be observed in the tundra environment (Royer et al., 2021a) and might add complexity to the snowpack microwave emission. In fact, Roy et al. (2015) observed a decrease in horizontal polarization as the impact of ice crust formation, but Roy et al. (2018) underlined the difficulty of modeling and quantifying such event at L-band. As for the vegetation, multiple effects may mitigate the T_g. The presence of shrubs leads to a snow accumulation with a lower density than on herbaceous areas, which means more thermal insulation from the snowpack (Grünberg et al., 2020; Liston et al., 2002). However, Domine et al. (2022) also observed thermal exchanges between air and soil through the branches. As these effects are observed at local scale, it is difficult to model it at the SMOS scale ($\simeq 40$ km). Various temporal matching between *in situ* measurements $T_{g\text{-insitu}}$ and the retrieved T_g were tested (not shown): closest measurement to the satellite overpass time (Catherinot et al., 2011) or daily maximum, minimum (Jones et al., 2007) or mean. The metrics remained similar because we observed very few daily variations of T_g due to the snow insulation effect.

5.2 T_g retrievals under the snowpack for sites with $\nu_{wi} \geq 0.20$

For sites with $0.20 \leq \nu_{wi} \leq 0.41$, the retrievals showed a strong negative bias when ignoring the snow and ice covered water bodies with MEM$_G$. We corrected the bias with the model MEM$_{G+WI}$ accounting for water bodies' contribution by optimizing the $H_{r,wi}$ parameter. A single $H_{r,wi}$ value did not suit all the sites. Validating T_g retrievals for sites with water body fractions between 0.04 and 0.20 may help to understand the water bodies' effects in the retrievals and how to account for them. For sites with $\nu_{wi} \geq 0.44$, the bias was larger with MEM$_{G+WI}$ than with MEM$_G$. In fact, the bias could already be minimized using an appropriate $H_{r,gs}$. However, the correlation remained poor for these sites (R < 0.3). For ERA5, the bias median was larger for sites with $\nu_{wi} \geq 0.20$ (median = 1.0°C) than for sites with $\nu_{wi} \leq 0.04$ (median = -0.1°C). For sites with higher biases (namely Niguanak, Marsh Creek, Camden Bay and Fish Creek), no correlation could be made with surface characteristics, such as land cover (Table 1) and soil content (Table A1). However, we noticed that those sites correspond to coastal pixels, i.e. made of BT measured on the continent and the ocean. Kerr et al. (2020) highlighted the retrieval difficulties for coastal BT that result from mixed pixels. In fact, the observation geometry variations that lead to various water fractions are not taken into account in the MEM.

5.2.1 Effects of the snow and ice covered water bodies

We used the water fraction for a 40 km resolution, but Kerr et al. (2020) showed that a working area of ~ 123 km$\times 123$ km is required to capture all the microwave signal that contributes to the SMOS observed BT. In fact, due to the multiple observation angles, the size and shape of the elliptical footprint vary. Using an average single round buffer for all the angles is a potential error source. For sites located near the coast, the nearby presence of the ocean is non-negligible. The considered water body areas may also vary over time. Dynamic water maps could improve the T_B correction, even more if they provide us with information on the water state (e.g. frozen, snow and ice covered, etc.). The water bodies highly impact the passive microwaves

observations in summer in the Arctic area (Ortet et al., 2024). Including water bodies in the MEM in winter is even more difficult because even if their surface is fully covered with ice, they may not be completely frozen in depth (Lemmetyinen et al., 2011). We tested various modeling configurations for the water bodies (ice only, liquid water only, ice on top of liquid water with a smooth interface, not shown). None were fully satisfying, but introducing the $H_{\mathrm{r,wi}}$ parameter worked better. Indeed, it represents the surface roughness at the ice-water interface, which is not flat and significantly impacts microwave observations. Yet, different models should be applied depending on water bodies characteristics (e.g. depth) as shallower lakes could freeze down to bottom or sea ice may be formed on the coastal areas.

5.2.2 Analysis of a site with high water fraction (Inigok)

Figures 4 and 6 show that using a unique $H_{\mathrm{r,wi}}$ for all the sites does not allow to get fully optimized T_{g}. To better understand the possible impact of snow and ice covered water bodies and model configuration, we present the Inigok site with a high water fraction of $\nu_{\mathrm{wi}} = 0.23$. Figure 8 shows varying performance of the timeseries of $T_{\mathrm{g,MEM_G}}$, $T_{\mathrm{g,MEM_{G+WI}}}$ and $T_{\mathrm{g\text{-}ERA5}}$ compared to $T_{\mathrm{g\text{-}insitu}}$. The $T_{\mathrm{g,MEM_G}}$ time series showed a negative bias that was well corrected in the $T_{\mathrm{g,MEM_{G+WI}}}$ time series. The $T_{\mathrm{g\text{-}ERA5}}$ time series did not show a systematic bias with the $T_{\mathrm{g\text{-}insitu}}$ time series. However, the ERA5 dynamic was quite different from the *in situ* measurements. While $T_{\mathrm{g\text{-}insitu}}$ and T_{g} seemed linked to air temperature when it rises above -10°C (e.g. in early 2014), but with a lag. This was not observed for $T_{\mathrm{g\text{-}ERA5}}$, while it appeared in the retrieved $T_{\mathrm{g,MEM_G}}$ and $T_{\mathrm{g,MEM_{G+WI}}}$. This could be linked to wet snow events, that increase the snowpack thermal conductivity and consequently the link between air temperatures and T_{g}. They also challenge the snowpack transparency hypothesis (Kumawat et al., 2022), that could be not valid anymore, and could lead to an increase in the retrieved T_{g} values. Using $\mathrm{MEM_G}$ or $\mathrm{MEM_{G+WI}}$ did not affect the time series dynamic, as shown by the similar R and ubRMSD in Figure 6. However, a strong interannual difference is observed. In winter 2014, we found R = 0.46 for $T_{\mathrm{g\text{-}ERA5}}$, while we obtained R = 0.29 for both $T_{\mathrm{g,MEM_G}}$ and $T_{\mathrm{g,MEM_{G+WI}}}$ (see Figure C1 in the appendices). On the contrary, in winter 2019, a correlation of R = -0.03 is obtained with ERA5, while R = 0.61 using $\mathrm{MEM_G}$ or $\mathrm{MEM_{G+WI}}$. These discrepancies between years suggest that ice conditions change throughout the years and further ice parametrization would be needed to obtain satisfactory T_{g} retrievals for scenes with high water body fractions.

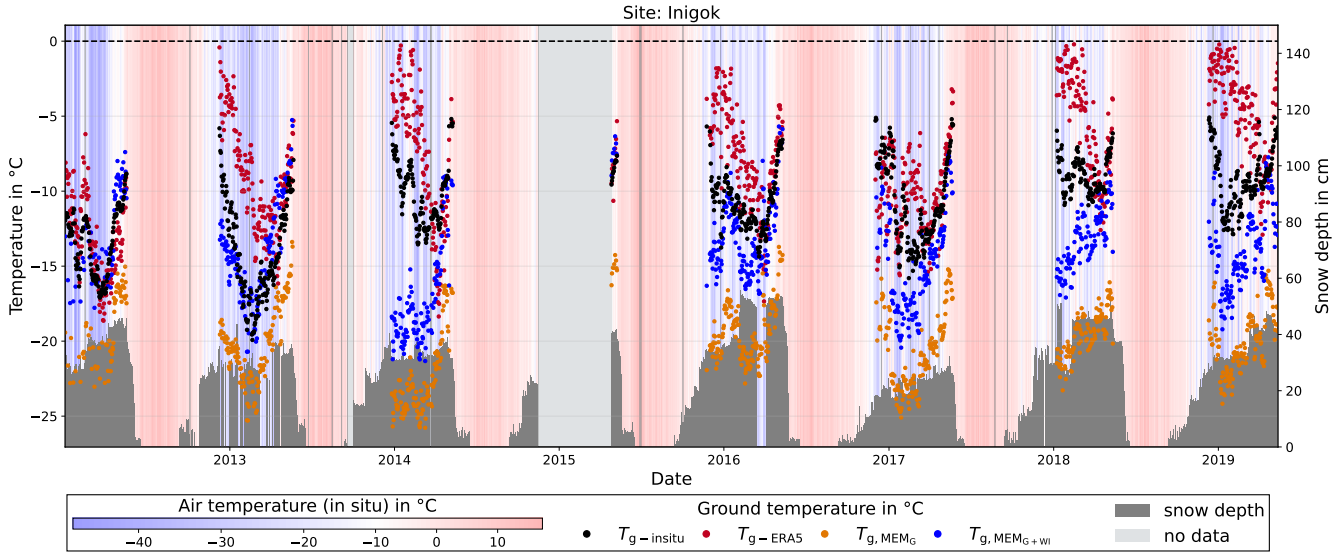

Figure 8. Time series of the ground temperatures (in °C, left axis) at Inigok from 2012 to 2020: $T_{\text{g-insitu}}$ (in black), $T_{\text{g,MEM}_{\text{G}}}$ (in orange), $T_{\text{g,MEM}_{\text{G+WI}}}$ (in blue) and $T_{\text{g-ERA5}}$ (in red). The snow depth (in cm, right axis) is displayed as dark grey bar plots. In the background, stripes from blue to red account for the *in situ* air temperature (in °C).

The similarities of behaviors of *in situ* and retrieved time series also varied during a single season. Figure 9 focuses on the retrievals using $\text{MEM}_{\text{G+WI}}$ with different $H_{\text{r,wi}}$ at Inigok from December 2016 to May 2017. This period corresponds to the winter season with best correlation according to Figure C1 (R = 0.74). The retrieved T_{g} and $T_{\text{g-insitu}}$ were averaged per month and plotted with their standard deviation. Each graph of Figure 9 corresponds to a different $H_{\text{r,wi}}$ used in the modeling. The difference between the monthly averaged T_{g} and the monthly averaged $T_{\text{g-insitu}}$ is noted $\Delta\bar{T}$. December ($\Delta\bar{T}$ = -0.5°C), January ($\Delta\bar{T}$ = -1.8°C) and February ($\Delta\bar{T}$ = 0°C) T_{g} are in good agreement with $T_{\text{g-insitu}}$ for $H_{\text{r,wi}}$ = 0.7. However, in March, $H_{\text{r,wi}}$ = 0.8 provide better results ($\Delta\bar{T}$ = -0.2°C). The best $H_{\text{r,wi}}$ is 0.9 for April ($\Delta\bar{T}$ = -0.5°C) and May ($\Delta\bar{T}$ = -0.5°C). This suggests a possible evolution of the ice conditions throughout the winter, that impacts the ice-water surface rugosity and T_{g} inversion. This is in agreement with SAR studies (Duguay and Lafleur, 2003; Murfitt et al., 2023) which take into account roughness parameters over lakes to represent the impact of the roughness at the water-ice interface on microwave signal. Murfitt et al. (2023) linked the water-ice interface roughness with the growth of tubular bubbles during ice formation, leading to higher roughness. Slushing water in ice cracks at the end of the freezing season induces more complexity than our three horizontal layers modeling for water bodies (Adams and Lasenby, 1985). Ground-based radiometric observations would be highly beneficial to better understand the seasonal effect of water-ice interface roughness on T_{B} in Arctic regions. Such observations may also help the development of a more complex model to better describe the L-band emissions of the circumarctic lakes and their variations through the seasons.

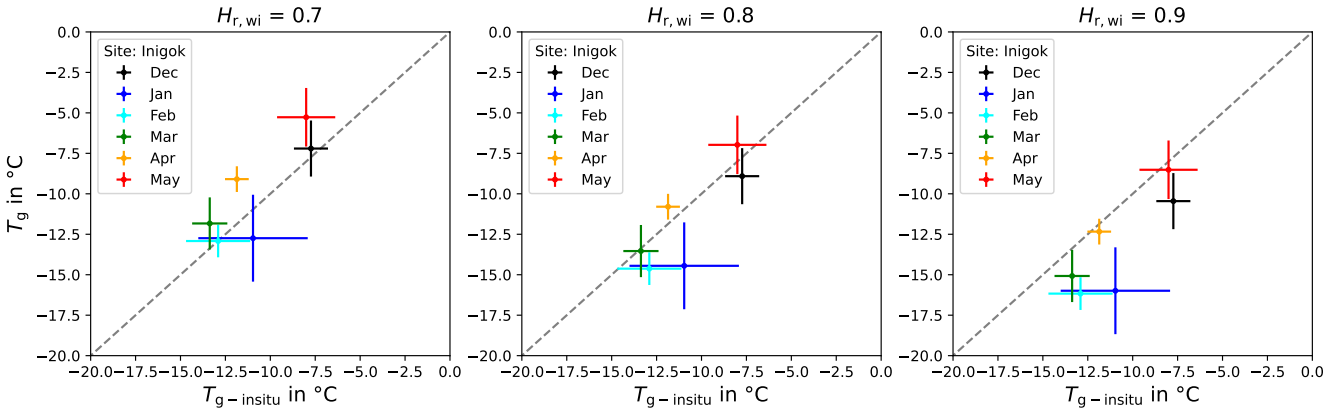

Figure 9. Scatter plots of the retrieved monthly average T_g (in °C) against *in situ* averaged $T_{g\text{-insitu}}$ (in °C) at the Inigok site from December 2016 to May 2017. The error bars show the standard deviation of the retrieved and measured temperatures. $H_{r,wi}$ values used in the inversion are 0.7 (left), 0.8 (middle), and 0.9 (right). The grey dashed line corresponds to the 1:1 identity line.

6 Conclusions

This study aimed to expand the previous studies on L-band passive microwave modeling and ground-based observations of snow-covered scenes by retrieving ground temperatures from satellite measurements in winter conditions. Our approach is based on SMOS L-band observations from 2012 to 2019. Two MEM configurations were explored to retrieve the T_g below the snowpack in the Arctic: one considering a homogeneous scene (MEM_G) and another one correcting the scene for the snow and ice covered water body fraction (MEM_{G+WI}). T_g retrieved with both MEM were validated with *in situ* measurements of 21 sites across northern Alaska and compared to $T_{g\text{-}ERA5}$. Several conclusions can be drawn from our results:

- T_g under the snowpack can be retrieved from SMOS observations with a relatively simple MEM and limited auxiliary data.
- For sites with low water fraction (≤ 0.04), T_g were retrieved with a median correlation R of 0.60 and a median bias of -0.2°C. For the same sites, the ERA5 median R was 0.51 and median bias was -0.8°C.
- For sites with a higher water fraction (≥ 0.20), ignoring the water fraction (MEM_G) leads to strong negative biases. The bias can be reduced using an ice-water roughness parameter $H_{r,wi}$, but correlation with *in situ* remains low (< 0.5 and worse than ERA5).
- Further work needs to be done to assess the impact of the snow and ice covered water bodies on L-band T_B evolving through the winter season.

With its launch in 2010, SMOS has offered observations for almost 15 years to this day. Producing T_{g} maps over the Arctic for the whole period would improve monitoring of the permafrost state in space and time and would be highly beneficial for carbon models.

Data availability. SMOS L3BT are openly available at https://dx.doi.org/10.12770/6294e08c-baec-4282-a251-33fee22ec67f. USGS *in situ* data was sourced from https://www.sciencebase.gov/catalog/item/59d6a458e4b05fe04cc6b47e. CARVE data is freely available on https://daac.ornl.gov/cgi-bin/dsviewer.pl?ds_id=1424. SCAN and SNOTEL data was sourced from ISMN at https://ismn.earth/en/dataviewer/#. ERA5 data are openly available on https://cds.climate.copernicus.eu/datasets/reanalysis-era5-single-levels?tab=download. The ESA CCI L4 map, Version 2.0.7 can be accessed at http://maps.elie.ucl.ac.be/CCI/viewer/download.php.

Appendix A: Soil properties

Table A1. Study sites soil characteristics at 0–5 cm extracted from SoilGrids 250 m v2.0 database (Poggio et al. 2021).

Network	Site	Clay (%)	Sand (%)	Silt (%)	SOC (g kg^{-1})	Bulk density (g cm^{-3})
CARVE	Atqasuk	14.1	67.2	18.7	402.3	0.33
	Barrow	28.3	37.8	33.9	360.7	0.51
	Ivotuk	25.4	29.3	45.3	384.3	0.43
USGS	Inigok	20.6	34.9	44.4	310.8	0.42
	Fish Creek	17.6	40	42.4	331.3	0.38
	Umiat	24	20	56	389.7	0.41
	Tunalik	20.3	31	48.7	331.3	0.45
	Koluktak	23.3	27.6	49.1	327.9	0.41
	Niguanak	19.8	31.8	48.3	279.3	0.47
	Marsh Creek	18.1	27.6	54.3	290.6	0.41
	South Meade	16.7	51.9	31.4	377.5	0.36
	Camden Bay	23	32.3	44.7	24.8	0.66
	Awuna2	25.2	22.3	52.5	348.2	0.44
	Piksiksak	19.3	32.9	47.8	353.6	0.44
	East Teshekpuk	23.6	43.8	32.7	312.5	0.39
	Ikpikpuk	21.1	40.9	38.1	335.6	0.41
ISMN SNOTEL	Imnaviat Creek	16.7	41.6	41.7	337.2	0.35
	Kelly Station	14.5	30.2	55.3	286	0.55
	Atigun Pass	25	46	29	129.7	0.65
ISMN SCAN	Ikalukrok Creek	18.2	40.3	41.5	287	0.62

Table A2. Frozen soil permittivity $\varepsilon_{\mathrm{frozen}}$ obtained from various dielectric constant models. No unfrozen water is considered, i.e. SM $= 0\ \mathrm{m}^3\ \mathrm{m}^{-3}$. When needed, the other soil properties are from SoilGrid 250 m v2.0 (Poggio et al., 2021) (Table A1). Note that the sign before the imagery part depends on different conventions.

Network	Site	Mironov et al. (2009)	Mironov et al. (2015)	Park et al. (2017)	Park et al. (2019)
CARVE	Atqasuk	2.36 + 0.11 i	1.45 + 0.04 i	2.22 + 0.07 i	1.91 + 0.06 i
	Barrow	2.15 + 0.08 i	1.73 + 0.06 i	2.07 + 0.07 i	2.17 + 0.08 i
	Ivotuk	2.19 + 0.09 i	1.60 + 0.05 i	2.36 + 0.09 i	2.23 + 0.09 i
USGS	Inigok	2.26 + 0.10 i	1.59 + 0.05 i	2.33 + 0.09 i	2.18 + 0.09 i
	Fish Creek	2.30 + 0.10 i	1.53 + 0.04 i	2.39 + 0.10 i	2.13 + 0.08 i
	Umiat	2.21 + 0.09 i	1.57 + 0.05 i	2.50 + 0.11 i	2.31 + 0.10 i
	Tunalik	2.26 + 0.10 i	1.64 + 0.05 i	2.29 + 0.09 i	2.21 + 0.09 i
	Koluktak	2.22 + 0.09 i	1.57 + 0.05 i	2.43 + 0.10 i	2.25 + 0.09 i
	Niguanak	2.27 + 0.10 i	1.67 + 0.06 i	2.22 + 0.09 i	2.21 + 0.09 i
	Marsh Creek	2.30 + 0.10 i	1.57 + 0.05 i	2.43 + 0.11 i	2.23 + 0.09 i
	South Meade	2.32 + 0.10 i	1.50 + 0.04 i	2.32 + 0.09 i	2.04 + 0.07 i
	Camden Bay	2.22 + 0.09 i	1.98 + 0.09 i	1.71 + 0.06 i	2.24 + 0.09 i
	Awuna2	2.19 + 0.09 i	1.62 + 0.05 i	2.39 + 0.10 i	2.29 + 0.10 i
	Piksiksak	2.28 + 0.10 i	1.62 + 0.05 i	2.30 + 0.09 i	2.19 + 0.09 i
	East Teshekpuk	2.21 + 0.09 i	1.54 + 0.05 i	2.33 + 0.09 i	2.12 + 0.07 i
	Ikpikpuk	2.25 + 0.09 i	1.57 + 0.05 i	2.30 + 0.09 i	2.14 + 0.08 i
	Lake 145	2.23 + 0.09 i	1.72 + 0.06 i	2.05 + 0.07 i	2.12 + 0.08 i
ISMN SNOTEL	Imnaviat Creek	2.32 + 0.10 i	1.48 + 0.04 i	2.45 + 0.10 i	2.12 + 0.08 i
	Kelly Station	2.36 + 0.10 i	1.80 + 0.07 i	2.02 + 0.08 i	2.20 + 0.09 i
	Atigun Pass	2.19 + 0.09 i	1.97 + 0.09 i	1.66 + 0.05 i	2.12 + 0.07 i
ISMN SCAN	Ikalukrok Creek	2.29 + 0.10 i	1.92 + 0.08 i	1.77 + 0.06 i	2.14 + 0.08 i

Appendix B: Results: Figures with confidence intervals

The Figures B1, B2 and B3 below are respectively similar to the Figures 5, 6 and 7 but with the confidence intervals (CI) of each metric. The 5% and 95% CI are respectively represented in orange and blue, the metric in grey. As for each metric, the CI distribution of all sites is represented with a boxplot.

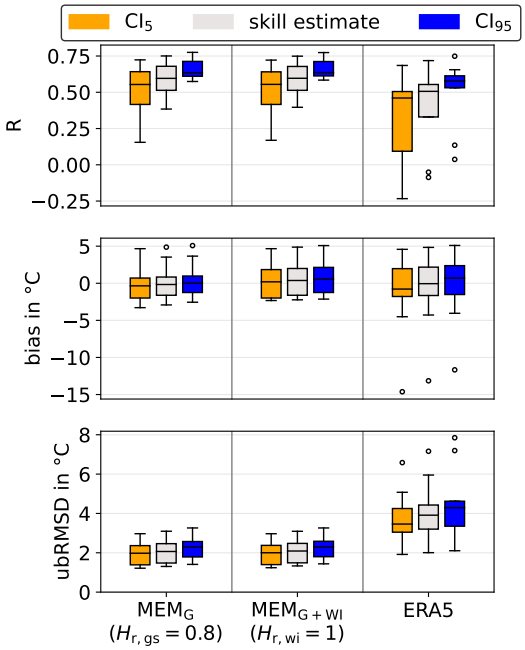

Figure B1. Summary statistics of R, bias and ubRMSD for sites with $\nu_{\mathrm{wi}} \leq 0.04$. The boxes show the median and interquartile range and whiskers show the 5 and 95 percentiles obtained from all the considered sites. The grey box corresponds to the skill estimate (R, bias, or ubRMSD). Respectively, the orange and blue boxes correspond to the associated 5% and 95% confidence interval limits obtained from all the considered sites. The x-axis corresponds to the $H_{\mathrm{r,wi}}$ used in the inversion. The boxes are respectively obtained from: $\mathrm{MEM_G}$ with $H_{\mathrm{r,gs}}$ = 8 (left), $\mathrm{MEM_{G+WI}}$ with $H_{\mathrm{r,wi}}$ = 1 (center) and ERA5 (right).

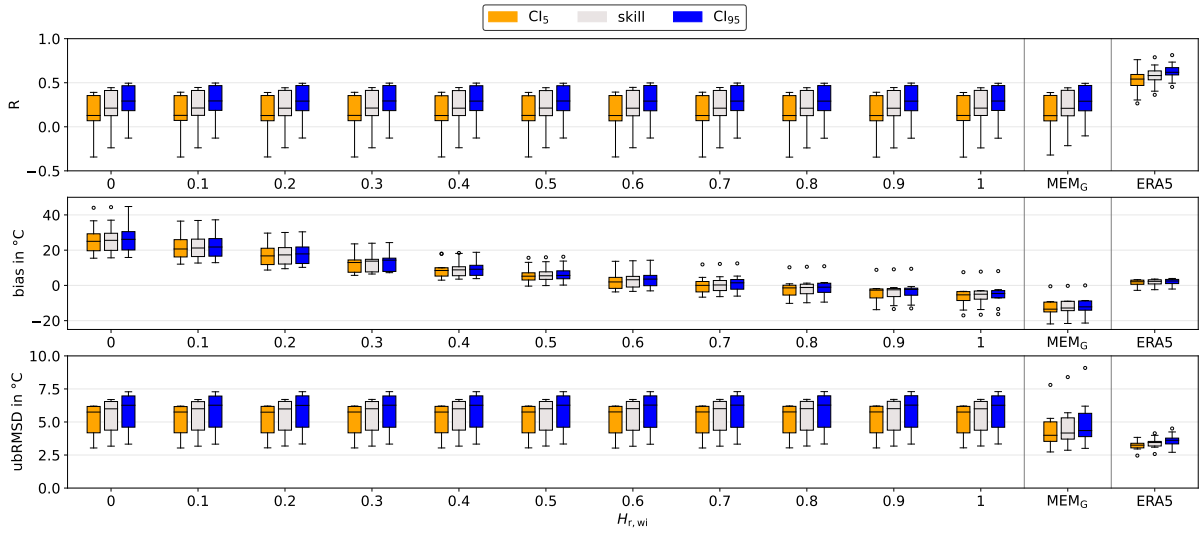

Figure B2. Summary statistics (in grey) of R, bias and ubRMSD and their 5% (in orange) and 95% (in blue) confidence intervals for sites with $0.20 \leq \nu_{\mathrm{wi}} \leq 0.41$. Boxes represent the site median and interquartile range (Q_3 - Q_1) and whiskers represent the 5 and 95 percentiles. The x-axis corresponds to the $H_{\mathrm{r,wi}}$ used in the inversion. The rightmost boxes are obtained with ERA5.

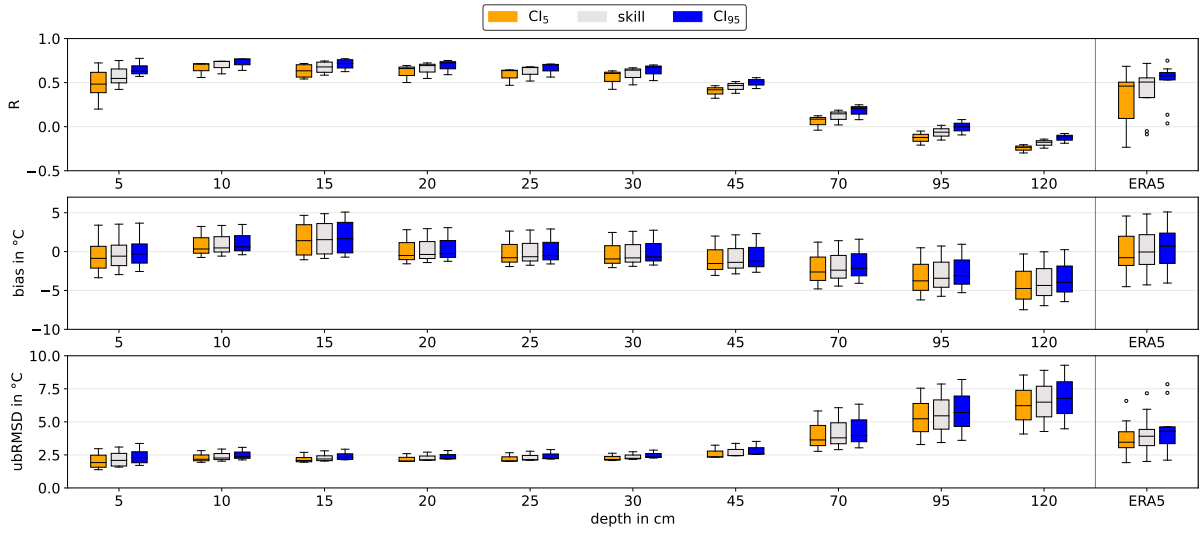

Figure B3. Summary statistics (in grey) of R, bias and ubRMSD and their 5% (in orange) and 95% (in blue) confidence intervals for sites with $\nu_{\mathrm{wi}} \leq 0.04$. Boxes represent the site median and interquartile range (Q_3 - Q_1) and whiskers represent the 5 and 95 percentiles. The x-axis corresponds to the *in situ* probing depths used for the validation. The extreme right boxes are obtained with ERA5 and $T_{\mathrm{g\text{-}insitu}}$ at 5 cm depth.

Appendix C: Case study: Inigok

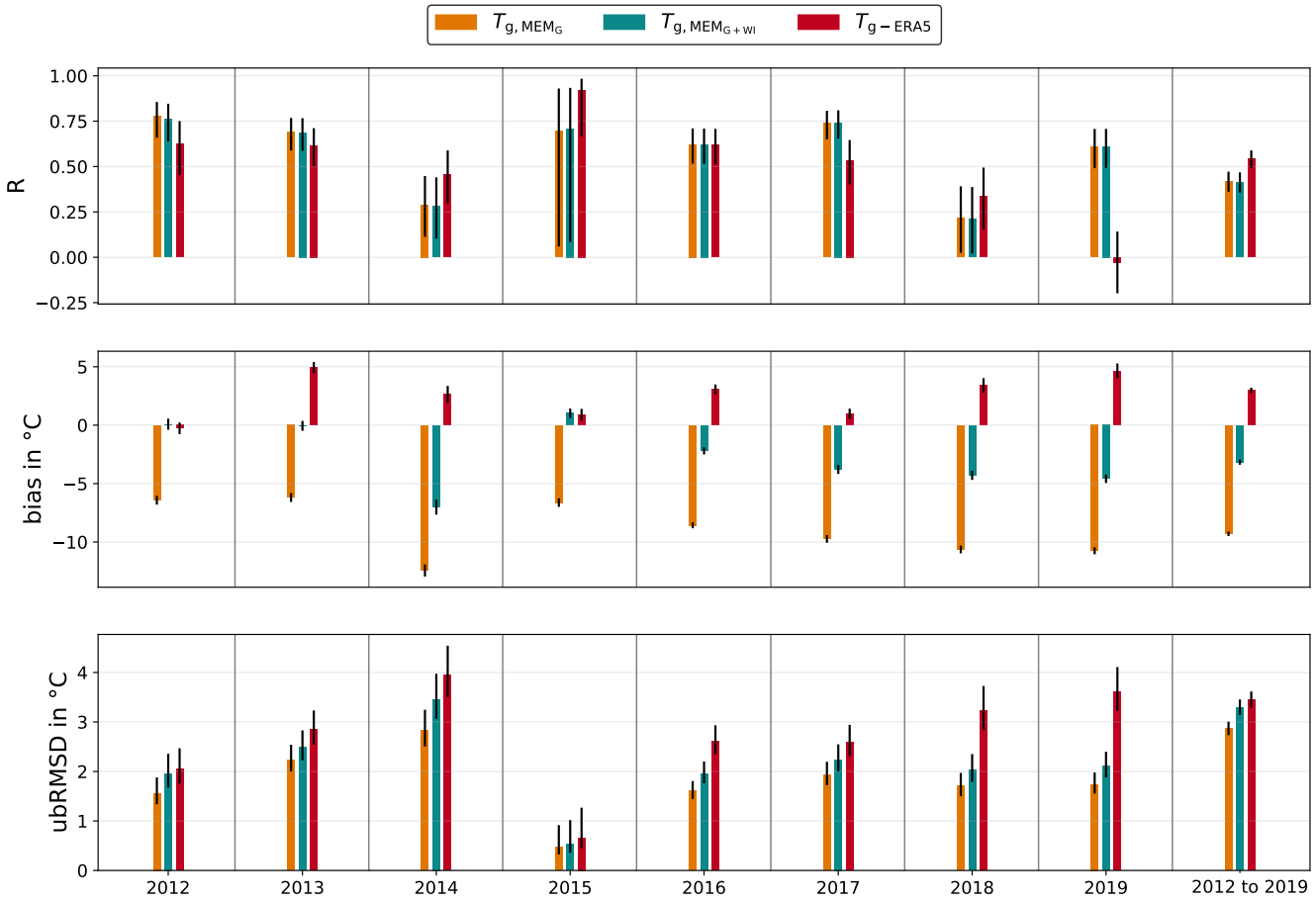

Figure C1. Yearly metrics obtained at Inigok from 2012 to 2020: $T_{\mathrm{g,MEM_G}}$ (in orange), $T_{\mathrm{g,MEM_{G+WI}}}$ (in blue) and $T_{\mathrm{g\text{-}ERA5}}$ (in red). R, bias and ubRMSD are plotted as bar plots, with error bars accounting for their 5% and 95% confidence intervals. On the far right, we show the global metrics obtained for the whole timeseries.

Appendix D: Summarizing performances

Table D1. Biases in °C for all sites (lines) and all H_{r} (columns). The last column gathers scores from ERA5. The sub-table on top corresponds to the model $\mathrm{MEM_G}$ and the one bellow to the model $\mathrm{MEM_G}$. The smallest bias obtained with $\mathrm{MEM_G}$ or $\mathrm{MEM_{G+WI}}$ per site (i.e. line) is in bold.

	Bias in °C											
	$\mathrm{MEM_G}$											ERA5
$H_{\mathrm{r,gs}}$	0	0.1	0.2	0.3	0.4	0.5	0.6	0.7	0.8	0.9	1	
Awuna2	18.0	15.6	13.5	11.7	10.0	8.5	7.2	5.9	4.9	3.9	**3.0**	1.8
Camden Bay	11.5	9.2	7.2	5.4	3.7	2.3	1.0	**-0.2**	-1.3	-2.2	-3.0	0.8
East Teshekpuk	**-9.8**	-11.9	-13.8	-15.5	-17.0	-18.3	-19.5	-20.6	-21.6	-22.5	-23.3	3.5
Fish Creek	6.1	3.9	1.8	**0.1**	-1.5	-3.0	-4.3	-5.4	-6.5	-7.4	-8.3	0.6
Ikpikpuk	**-6.4**	-8.6	-10.5	-12.2	-13.7	-15.1	-16.3	-17.4	-18.4	-19.3	-20.1	2.3
Inigok	3.1	**0.9**	-1.1	-2.8	-4.4	-5.8	-7.1	-8.3	-9.3	-10.2	-11.1	3.0
Koluktak	3.5	1.2	**-0.7**	-2.5	-4.1	-5.5	-6.8	-8.0	-9.0	-9.9	-10.8	0.8
Lake 145	**-2.1**	-4.3	-6.2	-8.0	-9.5	-10.9	-12.2	-13.3	-14.3	-15.2	-16.0	3.2
Marsh Creek	9.1	6.9	4.8	3.0	1.4	**-0.1**	-1.4	-2.5	-3.6	-4.5	-5.4	-0.8
Niguanak	12.6	10.3	8.2	6.4	4.8	3.3	2.0	0.8	**-0.3**	-1.2	-2.1	-1.1
Piksiksak	13.6	11.3	9.3	7.5	5.8	4.3	3.0	1.8	**0.8**	-0.2	-1.0	3.2
South Meade	3.3	1.1	**-0.9**	-2.6	-4.2	-5.6	-6.9	-8.0	-9.0	-9.9	-10.8	3.6
Tunalik	12.6	10.3	8.3	6.5	4.8	3.4	2.1	0.9	**-0.2**	-1.1	-2.0	4.8
Umiat	16.6	14.3	12.2	10.3	8.6	7.2	5.8	4.6	3.5	2.6	**1.7**	2.2
Atqasuk	**-0.7**	-2.9	-4.9	-6.6	-8.2	-9.6	-10.9	-12.0	-13.0	-13.9	-14.8	1.1
Barrow	**-1.9**	-4.1	-6.0	-7.8	-9.3	-10.7	-12.0	-13.1	-14.1	-15.0	-15.8	-2.4
Ivotuk	11.4	9.0	7.0	5.1	3.5	2.0	0.6	**-0.5**	-1.6	-2.6	-3.4	-0.1
Atigun Pass	10.3	8.0	6.0	4.1	2.5	1.0	**-0.3**	-1.5	-2.5	-3.5	-4.4	-1.7
Ikalukrok Creek	11.8	9.5	7.4	5.6	4.0	2.5	1.2	**0.0**	-1.1	-2.1	-2.9	-0.2
Imnaviat Creek	13.9	11.6	9.5	7.7	6.0	4.5	3.1	1.9	0.8	-0.1	-1.0	-4.3
Kelly Station	10.1	7.7	5.7	3.8	2.2	0.7	**-0.6**	-1.8	-2.9	-3.8	-4.8	-13.1

	Bias in °C											
	$\mathrm{MEM_{G+WI}}$											ERA5
$H_{\mathrm{r,wi}}$	0	0.1	0.2	0.3	0.4	0.5	0.6	0.7	0.8	0.9	1	
Awuna2	4.9	4.9	4.9	4.9	4.9	4.9	4.9	4.9	4.9	4.9	4.9	1.8
Camden Bay	79.7	70.5	62.1	54.6	47.8	41.7	36.2	31.3	26.8	22.7	**19.1**	0.8
East Teshekpuk	37.0	28.8	21.4	14.8	8.8	3.4	**-1.5**	-5.9	-9.8	-13.4	-16.7	3.5
Fish Creek	137.4	120.4	105.1	91.4	79.0	67.7	57.6	48.5	40.3	32.9	**26.2**	0.6
Ikpikpuk	22.7	17.1	12.1	7.6	3.6	-0.1	-3.4	-6.4	-9.1	-11.5	-13.7	2.3
Inigok	19.9	16.4	13.2	10.3	7.8	5.4	3.4	1.5	**-0.2**	-1.8	-3.2	3.0
Koluktak	15.6	12.7	10.0	7.7	5.5	3.6	1.8	**0.2**	-1.2	-2.5	-3.7	0.8
Lake 145	44.4	36.8	30.0	23.9	18.4	13.4	9.0	4.9	**1.3**	-2.0	-5.0	3.2
Marsh Creek	77.4	68.2	59.8	52.3	45.5	39.4	33.9	29.0	24.5	20.4	**16.8**	-0.8
Niguanak	29.6	26.3	23.3	20.6	18.1	16.0	14.0	12.2	10.6	9.1	**7.8**	-1.1
Piksiksak	5.2	4.7	4.3	3.9	3.5	3.2	2.9	2.6	2.4	2.2	**2.0**	3.2
South Meade	25.6	21.2	17.3	13.8	10.6	7.7	5.1	2.8	**0.7**	-1.2	-3.0	3.6
Tunalik	2.0	1.7	1.5	1.3	1.1	1.0	0.8	0.7	0.6	0.5	**0.4**	4.8
Umiat	5.8	5.6	5.3	5.2	5.0	4.8	4.7	4.5	4.4	4.3	**4.2**	2.2
Atqasuk	16.5	12.8	9.5	6.5	3.7	1.3	**-0.9**	-2.9	-4.7	-6.3	-7.8	1.1
Barrow	29.3	23.7	18.7	14.2	10.2	6.5	3.2	**0.2**	-2.5	-4.9	-7.1	-2.4
Ivotuk	-1.6	-1.6	-1.6	-1.6	-1.6	-1.6	-1.6	-1.6	-1.6	-1.6	-1.6	-0.1
Atigun Pass	**-1.5**	-1.6	-1.7	-1.8	-1.9	-1.9	-2.0	-2.1	-2.1	-2.2	-2.2	-1.7
Ikalukrok Creek	-1.1	-1.1	-1.1	-1.1	-1.1	-1.1	-1.1	-1.1	-1.1	-1.1	-1.1	-0.2
Imnaviat Creek	2.0	1.9	1.7	1.7	1.6	1.5	1.4	1.4	1.3	**1.2**	**1.2**	-4.3
Kelly Station	0.5	**0.1**	-0.2	-0.5	-0.7	-1.0	-1.2	-1.4	-1.6	-1.8	-1.9	-13.1

Table D2. R for all sites (lines) and all H_{r} (columns). The last column gathers scores from ERA5. The sub-table on top corresponds to the model $\mathrm{MEM_G}$ and the one bellow to the model $\mathrm{MEM_G}$.

	R											
	$\mathrm{MEM_G}$											ERA5
$H_{\mathrm{r,gs}}$	0	0.1	0.2	0.3	0.4	0.5	0.6	0.7	0.8	0.9	1	
Awuna2	0.64	0.63	0.63	0.63	0.63	0.63	0.63	0.63	0.63	0.63	0.63	0.55
Camden Bay	0.30	0.30	0.29	0.29	0.30	0.30	0.29	0.29	0.29	0.29	0.29	0.78
East Teshekpuk	0.13	0.13	0.13	0.13	0.13	0.13	0.12	0.13	0.12	0.13	0.13	0.58
Fish Creek	0.24	0.24	0.23	0.23	0.24	0.23	0.23	0.24	0.24	0.23	0.23	0.74
Ikpikpuk	0.35	0.35	0.35	0.35	0.35	0.35	0.35	0.35	0.35	0.35	0.35	0.70
Inigok	0.42	0.42	0.42	0.42	0.42	0.42	0.42	0.42	0.42	0.42	0.42	0.54
Koluktak	0.45	0.45	0.45	0.45	0.45	0.45	0.45	0.45	0.44	0.45	0.44	0.63
Lake 145	0.16	0.15	0.15	0.15	0.15	0.15	0.15	0.15	0.15	0.15	0.15	0.61
Marsh Creek	0.23	0.23	0.23	0.23	0.23	0.22	0.22	0.22	0.22	0.23	0.22	0.63
Niguanak	0.42	0.42	0.42	0.42	0.41	0.41	0.41	0.41	0.41	0.41	0.41	0.79
Piksiksak	0.74	0.74	0.74	0.74	0.73	0.74	0.74	0.74	0.74	0.74	0.74	0.51
South Meade	0.22	0.21	0.21	0.21	0.21	0.21	0.21	0.21	0.21	0.21	0.21	0.53
Tunalik	0.75	0.75	0.75	0.75	0.75	0.75	0.75	0.75	0.75	0.75	0.75	0.55
Umiat	0.60	0.60	0.60	0.60	0.60	0.60	0.60	0.59	0.60	0.60	0.59	0.62
Atqasuk	-0.24	-0.24	-0.24	-0.23	-0.23	-0.23	-0.23	-0.23	-0.24	-0.24	-0.24	0.40
Barrow	0.05	0.05	0.05	0.05	0.06	0.06	0.06	0.06	0.06	0.06	0.06	0.36
Ivotuk	0.50	0.49	0.50	0.49	0.50	0.49	0.49	0.49	0.49	0.49	0.50	-0.05
Atigun Pass	0.68	0.68	0.68	0.68	0.68	0.68	0.68	0.68	0.68	0.68	0.68	0.72
Ikalukrok Creek	0.51	0.51	0.51	0.51	0.51	0.51	0.51	0.51	0.51	0.51	0.51	-0.09
Imnaviat Creek	0.55	0.55	0.54	0.55	0.54	0.54	0.54	0.54	0.54	0.54	0.54	0.50
Kelly Station	0.41	0.40	0.40	0.39	0.41	0.41	0.41	0.40	0.38	0.41	0.39	0.33

	R											
	$\mathrm{MEM_{G+WI}}$											ERA5
$H_{\mathrm{r,wi}}$	0	0.1	0.2	0.3	0.4	0.5	0.6	0.7	0.8	0.9	1	
Awuna2	0.63	0.63	0.63	0.63	0.63	0.63	0.63	0.63	0.63	0.63	0.63	0.55
Camden Bay	0.29	0.29	0.29	0.29	0.29	0.29	0.29	0.29	0.29	0.29	0.29	0.78
East Teshekpuk	0.13	0.13	0.13	0.13	0.13	0.13	0.13	0.13	0.13	0.13	0.13	0.58
Fish Creek	0.24	0.24	0.24	0.24	0.24	0.24	0.24	0.24	0.24	0.24	0.24	0.74
Ikpikpuk	0.35	0.35	0.35	0.35	0.35	0.36	0.35	0.35	0.35	0.35	0.35	0.70
Inigok	0.41	0.41	0.41	0.41	0.42	0.42	0.42	0.42	0.42	0.42	0.41	0.54
Koluktak	0.44	0.45	0.44	0.44	0.45	0.44	0.45	0.45	0.44	0.45	0.44	0.63
Lake 145	0.16	0.15	0.16	0.15	0.15	0.15	0.15	0.15	0.15	0.15	0.15	0.61
Marsh Creek	0.23	0.23	0.23	0.24	0.23	0.23	0.22	0.22	0.22	0.23	0.22	0.63
Niguanak	0.41	0.41	0.41	0.41	0.41	0.41	0.41	0.41	0.41	0.41	0.41	0.79
Piksiksak	0.74	0.74	0.74	0.74	0.74	0.74	0.74	0.74	0.74	0.74	0.74	0.51
South Meade	0.21	0.21	0.21	0.21	0.21	0.21	0.21	0.21	0.21	0.21	0.21	0.53
Tunalik	0.75	0.75	0.75	0.75	0.75	0.75	0.75	0.75	0.75	0.75	0.75	0.55
Umiat	0.60	0.60	0.60	0.60	0.60	0.59	0.60	0.60	0.60	0.60	0.60	0.62
Atqasuk	-0.24	-0.24	-0.24	-0.24	-0.24	-0.24	-0.24	-0.24	-0.24	-0.24	-0.24	0.40
Barrow	0.06	0.06	0.06	0.06	0.06	0.06	0.06	0.06	0.06	0.06	0.06	0.36
Ivotuk	0.49	0.49	0.49	0.49	0.49	0.49	0.49	0.49	0.49	0.49	0.49	-0.05
Atigun Pass	0.68	0.68	0.68	0.68	0.68	0.68	0.68	0.68	0.68	0.68	0.68	0.72
Ikalukrok Creek	0.51	0.51	0.51	0.51	0.51	0.51	0.51	0.51	0.51	0.51	0.51	-0.09
Imnaviat Creek	0.54	0.54	0.54	0.54	0.54	0.54	0.54	0.54	0.54	0.54	0.54	0.50
Kelly Station	0.42	0.41	0.41	0.41	0.43	0.40	0.40	0.41	0.40	0.40	0.40	0.33

Table D3. ubRMSD in °C for all sites (lines) and all H_{r} (columns). The last column gathers scores from ERA5. The sub-table on top corresponds to the model $\mathrm{MEM_G}$ and the one bellow to the model $\mathrm{MEM_G}$.

	ubRMSD in °C											
	$\mathrm{MEM_G}$											ERA5
$H_{\mathrm{r,gs}}$	0	0.1	0.2	0.3	0.4	0.5	0.6	0.7	0.8	0.9	1	
Awuna2	2.3	2.3	2.3	2.3	2.3	2.3	2.3	2.3	2.3	2.3	2.3	3.2
Camden Bay	4.6	4.6	4.6	4.6	4.5	4.5	4.5	4.5	4.5	4.5	4.5	2.7
East Teshekpuk	4.4	4.3	4.3	4.3	4.3	4.3	4.3	4.3	4.2	4.2	4.2	3.5
Fish Creek	3.8	3.8	3.8	3.8	3.8	3.8	3.7	3.7	3.7	3.7	3.7	2.3
Ikpikpuk	3.8	3.8	3.8	3.8	3.8	3.8	3.8	3.8	3.8	3.8	3.8	3.2
Inigok	2.9	2.9	2.9	2.9	2.9	2.9	2.9	2.9	2.9	2.9	2.9	3.4
Koluktak	2.9	2.9	2.9	2.9	2.9	2.9	2.9	2.9	2.9	2.9	2.9	3.1
Lake 145	4.3	4.3	4.3	4.2	4.2	4.2	4.2	4.2	4.2	4.2	4.2	3.3
Marsh Creek	4.4	4.4	4.4	4.4	4.4	4.4	4.4	4.4	4.3	4.3	4.3	2.9
Niguanak	3.8	3.8	3.8	3.7	3.7	3.7	3.7	3.7	3.7	3.7	3.7	2.6
Piksiksak	2.5	2.5	2.5	2.5	2.5	2.5	2.5	2.5	2.5	2.5	2.5	4.1
South Meade	5.4	5.4	5.4	5.4	5.4	5.3	5.3	5.3	5.3	5.3	5.3	4.0
Tunalik	3.1	3.1	3.1	3.1	3.1	3.1	3.1	3.1	3.1	3.1	3.1	4.4
Umiat	2.1	2.1	2.1	2.1	2.1	2.1	2.1	2.1	2.1	2.1	2.1	3.2
Atqasuk	5.8	5.8	5.7	5.7	5.7	5.7	5.7	5.6	5.6	5.6	5.6	4.1
Barrow	8.3	8.2	8.2	8.2	8.1	8.1	8.1	8.0	8.0	8.0	8.0	3.5
Ivotuk	2.1	2.1	2.0	2.0	2.0	2.0	2.0	2.0	2.0	2.0	2.0	3.9
Atigun Pass	1.5	1.5	1.5	1.5	1.5	1.5	1.5	1.4	1.5	1.4	1.4	2.0
Ikalukrok Creek	3.0	3.0	3.0	3.0	3.0	3.0	3.0	3.0	3.0	3.0	3.0	7.2
Imnaviat Creek	1.4	1.4	1.3	1.3	1.3	1.3	1.3	1.3	1.3	1.3	1.3	2.2
Kelly Station	1.5	1.5	1.5	1.5	1.5	1.5	1.5	1.5	1.5	1.4	1.4	6.0

	ubRMSD in °C											
	$\mathrm{MEM_{G+WI}}$											ERA5
$H_{\mathrm{r,wi}}$	0	0.1	0.2	0.3	0.4	0.5	0.6	0.7	0.8	0.9	1	
Awuna2	2.3	2.3	2.3	2.3	2.3	2.3	2.3	2.3	2.3	2.3	2.3	3.2
Camden Bay	6.8	6.8	6.8	6.7	6.8	6.8	6.8	6.8	6.7	6.7	6.7	2.7
East Teshekpuk	6.1	6.1	6.1	6.2	6.1	6.1	6.1	6.1	6.1	6.1	6.1	3.5
Fish Creek	7.8	7.7	7.7	7.7	7.7	7.7	7.7	7.7	7.7	7.7	7.7	2.3
Ikpikpuk	4.4	4.4	4.4	4.4	4.4	4.4	4.4	4.4	4.4	4.4	4.4	3.2
Inigok	3.3	3.3	3.3	3.3	3.3	3.3	3.3	3.3	3.3	3.3	3.3	3.4
Koluktak	3.2	3.2	3.2	3.2	3.2	3.2	3.2	3.2	3.2	3.2	3.2	3.1
Lake 145	6.0	6.0	6.0	6.0	6.0	6.0	6.0	6.0	6.0	6.0	6.0	3.3
Marsh Creek	7.1	7.1	7.1	7.0	7.1	7.1	7.1	7.1	7.1	7.1	7.1	2.9
Niguanak	4.4	4.4	4.4	4.4	4.4	4.4	4.4	4.4	4.4	4.4	4.4	2.6
Piksiksak	2.5	2.5	2.5	2.5	2.5	2.5	2.5	2.5	2.5	2.5	2.5	4.1
South Meade	6.5	6.5	6.6	6.5	6.6	6.6	6.6	6.6	6.6	6.6	6.6	4.0
Tunalik	3.1	3.1	3.1	3.1	3.1	3.1	3.1	3.1	3.1	3.1	3.1	4.4
Umiat	2.1	2.1	2.1	2.1	2.1	2.1	2.1	2.1	2.1	2.1	2.1	3.2
Atqasuk	6.7	6.7	6.7	6.7	6.7	6.7	6.7	6.7	6.7	6.7	6.7	4.1
Barrow	11.5	11.5	11.5	11.5	11.5	11.5	11.5	11.5	11.5	11.5	11.5	3.5
Ivotuk	2.0	2.0	2.0	2.0	2.0	2.0	2.0	2.0	2.0	2.0	2.0	3.9
Atigun Pass	1.5	1.5	1.5	1.5	1.5	1.5	1.5	1.5	1.5	1.5	1.5	2.0
Ikalukrok Creek	3.0	3.0	3.0	3.0	3.0	3.0	3.0	3.0	3.0	3.0	3.0	7.2
Imnaviat Creek	1.3	1.3	1.3	1.4	1.4	1.3	1.3	1.4	1.3	1.3	1.3	2.2
Kelly Station	1.5	1.5	1.5	1.5	1.5	1.5	1.5	1.5	1.5	1.5	1.5	6.0

Author contributions. JO carried out this study by analyzing data, performing the inversions, and organizing and writing the paper. ARoyer, AM and ARoy proposed the initial idea. MS and MH provided expertise in microwave emission model and contributed to the writing of the manuscript. All the authors were involved in the analysis of the results and contributed to the writing of the paper.

Competing interests. The authors declare no conflict of interest.

Acknowledgements. This work was funded by the CNES (Centre National d'Etudes Spatiales) through J.O. PhD funding (contract no. JC.2O2O.OO39O41) and the Science TOSCA (Terre Océan Surfaces Continentales et Atmosphère) program. The authors acknowledge the support of the Natural Sciences and Engineering Research Council of Canada (NSERC). This study has been partially supported through the grant EUR TESS N°ANR-18-EURE-0018 in the framework of the Programme des Investissements d'Avenir. A contribution to this work was made at the Jet Propulsion Laboratory, California Institute of Technology, under a contract with the National Aeronautics and Space Administration.

References

ESA. Land Cover CCI Product User Guide Version 2.

Aalto, J., Karjalainen, O., Hjort, J., and Luoto, M.: Statistical Forecasting of Current and Future Circum-Arctic Ground Temperatures and Active Layer Thickness, Geophysical Research Letters, 45, 4889–4898, https://doi.org/10.1029/2018GL078007, 2018.

Adams, W. and Lasenby, D.: The Roles of Snow, Lake Ice and Lake Water in the Distribution of Major Ions in the Ice Cover of a Lake, Annals of Glaciology, 7, 202–207, https://doi.org/10.3189/S0260305500006170, 1985.

Aksoy, M. and Johnson, J. T.: A Study of SMOS RFI Over North America, IEEE Geoscience and Remote Sensing Letters, 10, 515–519, https://doi.org/10.1109/LGRS.2012.2211993, 2013.

Al Bitar, A., Mialon, A., Kerr, Y. H., Cabot, F., Richaume, P., Jacquette, E., Quesney, A., Mahmoodi, A., Tarot, S., Parrens, M., Al-Yaari, A., Pellarin, T., Rodriguez-Fernandez, N., and Wigneron, J.-P.: The Global SMOS Level 3 Daily Soil Moisture and Brightness Temperature Maps, Earth System Science Data, 9, 293–315, https://doi.org/10.5194/essd-9-293-2017, 2017.

Ala-Aho, P., Autio, A., Bhattacharjee, J., Isokangas, E., Kujala, K., Marttila, H., Menberu, M., Meriö, L.-J., Postila, H., Rauhala, A., Ronkanen, A.-K., Rossi, P. M., Saari, M., Haghighi, A. T., and Kløve, B.: What Conditions Favor the Influence of Seasonally Frozen Ground on Hydrological Partitioning? A Systematic Review, Environmental Research Letters, 16, 043 008, https://doi.org/10.1088/1748-9326/abe82c, 2021.

André, C., Ottlé, C., Royer, A., and Maignan, F.: Land Surface Temperature Retrieval over Circumpolar Arctic Using SSM/I–SSMIS and MODIS Data, Remote Sensing of Environment, 162, 1–10, https://doi.org/10.1016/j.rse.2015.01.028, 2015.

Bartlett, M. G., Chapman, D. S., and Harris, R. N.: Snow and the Ground Temperature Record of Climate Change, Journal of Geophysical Research: Earth Surface, 109, 2004JF000 224, https://doi.org/10.1029/2004JF000224, 2004.

Bartsch, A., Bergstedt, H., Pointner, G., Muri, X., Rautiainen, K., Leppänen, L., Joly, K., Sokolov, A., Orekhov, P., Ehrich, D., and Soininen, E. M.: Towards Long-Term Records of Rain-on-Snow Events across the Arctic from Satellite Data, The Cryosphere, 17, 889–915, https://doi.org/10.5194/tc-17-889-2023, 2023.

Benninga, H.-J. F., Van Der Velde, R., and Su, Z.: Sentinel-1 Soil Moisture Content and Its Uncertainty over Sparsely Vegetated Fields, Journal of Hydrology X, 9, 100 066, https://doi.org/10.1016/j.hydroa.2020.100066, 2020.

Bircher, S., Demontoux, F., Razafindratsima, S., Zakharova, E., Drusch, M., Wigneron, J.-P., and Kerr, Y.: L-Band Relative Permittivity of Organic Soil Surface Layers—A New Dataset of Resonant Cavity Measurements and Model Evaluation, Remote Sensing, 8, 1024, https://doi.org/10.3390/rs8121024, 2016.

Biskaborn, B. K., Smith, S. L., Noetzli, J., Matthes, H., Vieira, G., Streletskiy, D. A., Schoeneich, P., Romanovsky, V. E., Lewkowicz, A. G., Abramov, A., Allard, M., Boike, J., Cable, W. L., Christiansen, H. H., Delaloye, R., Diekmann, B., Drozdov, D., Etzelmüller, B., Grosse, G., Guglielmin, M., Ingeman-Nielsen, T., Isaksen, K., Ishikawa, M., Johansson, M., Johannsson, H., Joo, A., Kaverin, D., Kholodov, A., Konstantinov, P., Kröger, T., Lambiel, C., Lanckman, J.-P., Luo, D., Malkova, G., Meiklejohn, I., Moskalenko, N., Oliva, M., Phillips, M., Ramos, M., Sannel, A. B. K., Sergeev, D., Seybold, C., Skryabin, P., Vasiliev, A., Wu, Q., Yoshikawa, K., Zheleznyak, M., and Lantuit, H.: Permafrost Is Warming at a Global Scale, Nature Communications, 10, 264, https://doi.org/10.1038/s41467-018-08240-4, 2019.

Brodzik, M. J., Billingsley, B., Haran, T., Raup, B., and Savoie, M. H.: EASE-Grid 2.0: Incremental but Significant Improvements for Earth-Gridded Data Sets, ISPRS International Journal of Geo-Information, 1, 32–45, https://doi.org/10.3390/ijgi1010032, 2012.

Cao, B., Gruber, S., Zheng, D., and Li, X.: The ERA5-Land Soil Temperature Bias in Permafrost Regions, The Cryosphere, 14, 2581–2595, https://doi.org/10.5194/tc-14-2581-2020, 2020.

CATDS: CATDS-PDC L3TB - Daily Global Polarised Brightness Temperature Product from SMOS Satellite, https://doi.org/10.12770/6294E08C-BAEC-4282-A251-33FEE22EC67F, 2024.

Catherinot, J., Prigent, C., Maurer, R., Papa, F., Jiménez, C., Aires, F., and Rossow, W. B.: Evaluation of "All Weather" Microwave-Derived Land Surface Temperatures with in Situ CEOP Measurements: "ALL WEATHER" LAND SURFACE TEMPERATURE EVALUATION, Journal of Geophysical Research: Atmospheres, 116, n/a–n/a, https://doi.org/10.1029/2011JD016439, 2011.

Chadburn, S. E., Burke, E. J., Cox, P. M., Friedlingstein, P., Hugelius, G., and Westermann, S.: An Observation-Based Constraint on Permafrost Loss as a Function of Global Warming, Nature Climate Change, 7, 340–344, https://doi.org/10.1038/nclimate3262, 2017.

Chaubell, M. J., Yueh, S. H., Dunbar, R. S., Colliander, A., Chen, F., Chan, S. K., Entekhabi, D., Bindlish, R., O'Neill, P. E., Asanuma, J., Berg, A. A., Bosch, D. D., Caldwell, T., Cosh, M. H., Holifield Collins, C., Martinez-Fernandez, J., Seyfried, M., Starks, P. J., Su, Z., Thibeault, M., and Walker, J.: Improved SMAP Dual-Channel Algorithm for the Retrieval of Soil Moisture, IEEE Transactions on Geoscience and Remote Sensing, 58, 3894–3905, https://doi.org/10.1109/TGRS.2019.2959239, 2020.

Choudhury, B. J., Schmugge, T. J., Chang, A., and Newton, R. W.: Effect of Surface Roughness on the Microwave Emission from Soils, Journal of Geophysical Research: Oceans, 84, 5699–5706, https://doi.org/10.1029/JC084iC09p05699, 1979.

Daganzo-Eusebio, E., Oliva, R., Kerr, Y. H., Nieto, S., Richaume, P., and Mecklenburg, S. M.: SMOS Radiometer in the 1400–1427-MHz Passive Band: Impact of the RFI Environment and Approach to Its Mitigation and Cancellation, IEEE Transactions on Geoscience and Remote Sensing, 51, 4999–5007, https://doi.org/10.1109/TGRS.2013.2259179, 2013.

Defourny, P., Lamarche, C., Brockmann, C., Boettcher, M., Bontemps, S., De Maet, T., Duveiller, G. L., Harper, K., Hartley A., Kirches, G., Moreau, I., Peylin, P., Ottlé, C., Radoux J., Van Bogaert, E, Ramoino, F., Albergel, C., and Arino, O.: Observed Annual Global Land-Use Change from 1992 to 2020 Three Times More Dynamic than Reported by Inventory-Based Statistics, 2023.

Derksen, C., Lemmetyinen, J., Toose, P., Silis, A., Pulliainen, J., and Sturm, M.: Physical Properties of Arctic versus Subarctic Snow: Implications for High Latitude Passive Microwave Snow Water Equivalent Retrievals, Journal of Geophysical Research: Atmospheres, 119, 7254–7270, https://doi.org/10.1002/2013JD021264, 2014.

Dobiński, W.: Permafrost Active Layer, Earth-Science Reviews, 208, 103 301, https://doi.org/10.1016/j.earscirev.2020.103301, 2020.

Domine, F., Picard, G., Morin, S., Barrere, M., Madore, J.-B., and Langlois, A.: Major Issues in Simulating Some Arctic Snowpack Properties Using Current Detailed Snow Physics Models: Consequences for the Thermal Regime and Water Budget of Permafrost, Journal of Advances in Modeling Earth Systems, 11, 34–44, https://doi.org/10.1029/2018MS001445, 2019.

Domine, F., Fourteau, K., Picard, G., Lackner, G., Sarrazin, D., and Poirier, M.: Permafrost Cooled in Winter by Thermal Bridging through Snow-Covered Shrub Branches, Nature Geoscience, 15, 554–560, https://doi.org/10.1038/s41561-022-00979-2, 2022.

Donlon, C., Galeazzi, C., Midthassel, R., Sallusti, M., Triggianese, M., Fiorelli, B., De Paris, G., Kornienko, A., and Khlystova, I.: The Copernicus Imaging Microwave Radiometer (CIMR): Mission Overview and Status, in: IGARSS 2023 - 2023 IEEE International Geoscience and Remote Sensing Symposium, pp. 989–992, IEEE, Pasadena, CA, USA, ISBN 9798350320107, https://doi.org/10.1109/IGARSS52108.2023.10281934, 2023.

Dorigo, W., Himmelbauer, I., Aberer, D., Schremmer, L., Petrakovic, I., Zappa, L., Preimesberger, W., Xaver, A., Annor, F., Ardö, J., Baldocchi, D., Bitelli, M., Blöschl, G., Bogena, H., Brocca, L., Calvet, J.-C., Camarero, J. J., Capello, G., Choi, M., Cosh, M. C., Van De Giesen, N., Hajdu, I., Ikonen, J., Jensen, K. H., Kanniah, K. D., De Kat, I., Kirchengast, G., Kumar Rai, P., Kyrouac, J., Larson, K., Liu, S., Loew, A., Moghaddam, M., Martínez Fernández, J., Mattar Bader, C., Morbidelli, R., Musial, J. P., Osenga, E., Palecki, M. A., Pellarin, T., Petropoulos, G. P., Pfeil, I., Powers, J., Robock, A., Rüdiger, C., Rummel, U., Strobel, M., Su, Z., Sullivan, R., Tagesson, T., Varlagin, A., Vreugdenhil, M., Walker, J., Wen, J., Wenger, F., Wigneron, J. P., Woods, M., Yang, K., Zeng, Y., Zhang, X., Zreda, M., Dietrich, S.,

Gruber, A., Van Oevelen, P., Wagner, W., Scipal, K., Drusch, M., and Sabia, R.: The International Soil Moisture Network: Serving Earth System Science for over a Decade, Hydrology and Earth System Sciences, 25, 5749–5804, https://doi.org/10.5194/hess-25-5749-2021, 2021.

Druckenmiller, M. L. and Jeffries, M.: December 2019 Www.Arctic.Noaa.Gov/Report-Card, 2019.

Duan, S.-B., Han, X.-J., Huang, C., Li, Z.-L., Wu, H., Qian, Y., Gao, M., and Leng, P.: Land Surface Temperature Retrieval from Passive Microwave Satellite Observations: State-of-the-Art and Future Directions, Remote Sensing, 12, 2573, https://doi.org/10.3390/rs12162573, 2020.

Duguay, C. R. and Lafleur, P. M.: Determining Depth and Ice Thickness of Shallow Sub-Arctic Lakes Using Space-Borne Optical and SAR Data, International Journal of Remote Sensing, 24, 475–489, https://doi.org/10.1080/01431160304992, 2003.

Entekhabi, D., Reichle, R. H., Koster, R. D., and Crow, W. T.: Performance Metrics for Soil Moisture Retrievals and Application Requirements, Journal of Hydrometeorology, 11, 832–840, https://doi.org/10.1175/2010JHM1223.1, 2010.

Escorihuela, M., Kerr, Y., De Rosnay, P., Wigneron, J.-P., Calvet, J.-C., and Lemaitre, F.: A Simple Model of the Bare Soil Microwave Emission at L-Band, IEEE Transactions on Geoscience and Remote Sensing, 45, 1978–1987, https://doi.org/10.1109/TGRS.2007.894935, 2007.

Fily, M.: A Simple Retrieval Method for Land Surface Temperature and Fraction of Water Surface Determination from Satellite Microwave Brightness Temperatures in Sub-Arctic Areas, Remote Sensing of Environment, 85, 328–338, https://doi.org/10.1016/S0034-4257(03)00011-7, 2003.

Gélinas, A., Filali, B., Langlois, A., Kelly, R., Mavrovic, A., Demontoux, F., and Roy, A.: New Wideband Large Aperture Open-Ended Coaxial Microwave Probe for Soil Dielectric Characterization, IEEE Transactions on Geoscience and Remote Sensing, pp. 1–1, https://doi.org/10.1109/TGRS.2025.3539532, 2025.

Gruber, A., De Lannoy, G., Albergel, C., Al-Yaari, A., Brocca, L., Calvet, J.-C., Colliander, A., Cosh, M., Crow, W., Dorigo, W., Draper, C., Hirschi, M., Kerr, Y., Konings, A., Lahoz, W., McColl, K., Montzka, C., Muñoz-Sabater, J., Peng, J., Reichle, R., Richaume, P., Rüdiger, C., Scanlon, T., Van Der Schalie, R., Wigneron, J.-P., and Wagner, W.: Validation Practices for Satellite Soil Moisture Retrievals: What Are (the) Errors?, Remote Sensing of Environment, 244, 111 806, https://doi.org/10.1016/j.rse.2020.111806, 2020.

Grünberg, I., Wilcox, E. J., Zwieback, S., Marsh, P., and Boike, J.: Linking Tundra Vegetation, Snow, Soil Temperature, and Permafrost, Biogeosciences, 17, 4261–4279, https://doi.org/10.5194/bg-17-4261-2020, 2020.

Guo, H., Zhu, W., Xiao, C., Zhao, C., and Chen, L.: High-Precision Estimation of Pan-Arctic Soil Surface Temperature from MODIS LST by Incorporating Multiple Environment Factors and Monthly-Based Modeling, International Journal of Applied Earth Observation and Geoinformation, 133, 104 114, https://doi.org/10.1016/j.jag.2024.104114, 2024.

Hallikainen, M., Ulaby, F., Dobson, M., El-rayes, M., and Wu, L.-k.: Microwave Dielectric Behavior of Wet Soil-Part 1: Empirical Models and Experimental Observations, IEEE Transactions on Geoscience and Remote Sensing, GE-23, 25–34, https://doi.org/10.1109/TGRS.1985.289497, 1985.

Heginbottom, J., Brown, J., Ferrians, O., and Melnikov, E.: Circum-Arctic Map of Permafrost and Ground-Ice Conditions, Version 2, https://doi.org/10.7265/SKBG-KF16, 2002.

Herrington, T. C., Fletcher, C. G., and Kropp, H.: Validation of Pan-Arctic Soil Temperatures in Modern Reanalysis and Data Assimilation Systems, The Cryosphere, 18, 1835–1861, https://doi.org/10.5194/tc-18-1835-2024, 2024.

Hersbach, H., Bell B., Berrisford, P., Biavati, G., Horányi, A., Muñoz Sabater, J., Nicolas, J., Peubey, C., Radu, R., Rozum, I., Schepers, D., Simmons, A., Soci, C, Dee, D., and Thépaut, J-N.: ERA5 Hourly Data on Single Levels from 1940 to Present, https://doi.org/10.24381/CDS.ADBB2D47, 2023.

Holmberg, M., Lemmetyinen, J., Schwank, M., Kontu, A., Rautiainen, K., Merkouriadi, I., and Tamminen, J.: Retrieval of Ground, Snow, and Forest Parameters from Space Borne Passive L Band Observations. A Case Study over Sodankylä, Finland, Remote Sensing of Environment, 306, 114 143, https://doi.org/10.1016/j.rse.2024.114143, 2024.

Jeffries, M. O., Morris, K., and Kozlenko, N.: Ice Characteristics and Processes, and Remote Sensing of Frozen Rivers and Lakes, in: Geophysical Monograph Series, edited by Duguay, C. R. and Pietroniro, A., pp. 63–90, American Geophysical Union, Washington, D. C., ISBN 978-1-118-66642-5 978-0-87590-428-3, https://doi.org/10.1029/163GM05, 2013.

Jiménez-Muñoz, J. C., Sobrino, J. A., Skoković, D., Mattar, C., and Cristóbal, J.: Land Surface Temperature Retrieval Methods From Landsat-8 Thermal Infrared Sensor Data, IEEE Geoscience and Remote Sensing Letters, 11, 1840–1843, https://doi.org/10.1109/LGRS.2014.2312032, 2014.

Jones, L., Kimball, J., McDonald, K., Chan, S., Njoku, E., and Oechel, W.: Satellite Microwave Remote Sensing of Boreal and Arctic Soil Temperatures From AMSR-E, IEEE Transactions on Geoscience and Remote Sensing, 45, 2004–2018, https://doi.org/10.1109/TGRS.2007.898436, 2007.

Kerr, Y., Al-Yaari, A., Rodriguez-Fernandez, N., Parrens, M., Molero, B., Leroux, D., Bircher, S., Mahmoodi, A., Mialon, A., Richaume, P., Delwart, S., Al Bitar, A., Pellarin, T., Bindlish, R., Jackson, T., Rüdiger, C., Waldteufel, P., Mecklenburg, S., and Wigneron, J.-P.: Overview of SMOS Performance in Terms of Global Soil Moisture Monitoring after Six Years in Operation, Remote Sensing of Environment, 180, 40–63, https://doi.org/10.1016/j.rse.2016.02.042, 2016a.

Kerr, Y., Reul, N., Martín-Neira, M., Drusch, M., Alvera-Azcarate, A., Wigneron, J.-P., and Mecklenburg, S.: ESA's Soil Moisture and Ocean Salinity Mission – Achievements and Applications after More than 6 Years in Orbit, Remote Sensing of Environment, 180, 1–2, https://doi.org/10.1016/j.rse.2016.03.020, 2016b.

Kerr, Y., Richaume, P., Waldteufel, P., Ferrazzoli, P., Wigneron, J. P., Schwank, M., and Rautiainen, K.: Algorithm Theoretical Basis Document ({ATBD}) for the SMOS Level 2 Soil Moisture Processor, Technical Report TN-ESL-SM-GS-0001-4b SM-ESL (CBSA), p. 145, 2020.

Kerr, Y. H., Waldteufel, P., Wigneron, J.-P., Delwart, S., Cabot, F., Boutin, J., Escorihuela, M.-J., Font, J., Reul, N., Gruhier, C., Juglea, S. E., Drinkwater, M. R., Hahne, A., Martín-Neira, M., and Mecklenburg, S.: The SMOS Mission: New Tool for Monitoring Key Elements Ofthe Global Water Cycle, Proceedings of the IEEE, 98, 666–687, https://doi.org/10.1109/JPROC.2010.2043032, 2010.

Köhn, J. and Royer, A.: Microwave Brightness Temperature as an Indicator of Near-Surface Air Temperature over Snow in Canadian Northern Regions, International Journal of Remote Sensing, 33, 1126–1138, https://doi.org/10.1080/01431161.2010.550643, 2012.

Konings, A. G., Piles, M., Rötzer, K., McColl, K. A., Chan, S. K., and Entekhabi, D.: Vegetation Optical Depth and Scattering Albedo Retrieval Using Time Series of Dual-Polarized L-band Radiometer Observations, Remote Sensing of Environment, 172, 178–189, https://doi.org/10.1016/j.rse.2015.11.009, 2016.

Kumawat, D., Olyaei, M., Gao, L., and Ebtehaj, A.: Passive Microwave Retrieval of Soil Moisture Below Snowpack at L-Band Using SMAP Observations, IEEE Transactions on Geoscience and Remote Sensing, 60, 1–16, https://doi.org/10.1109/TGRS.2022.3216324, 2022.

Lawrence, H., Wigneron, J.-P., Demontoux, F., Mialon, A., and Kerr, Y. H.: Evaluating the Semiempirical H– Q Model Used to Calculate the L-Band Emissivity of a Rough Bare Soil, IEEE Transactions on Geoscience and Remote Sensing, 51, 4075–4084, https://doi.org/10.1109/TGRS.2012.2226995, 2013.

Leavesley, G., David, O, Garen, D.C., Goodbody, A.G., Lea, J., Marron, T., Perkins, T., Strobel, M., and Tama, R.: A Modeling Framework for Improved Agricultural Water-Supply Forecasting, in: Joint Federal Interagency Hydrologic Modeling Conference, Las Vegas, 2010.

Leduc-Leballeur, M., Picard, G., Macelloni, G., Mialon, A., and Kerr, Y. H.: Melt in Antarctica Derived from Soil Moisture and Ocean Salinity (SMOS) Observations at L Band, The Cryosphere, 14, 539–548, https://doi.org/10.5194/tc-14-539-2020, 2020.

Lembrechts, J. J., Van Den Hoogen, J., Aalto, J., Ashcroft, M. B., De Frenne, P., Kemppinen, J., Kopecký, M., Luoto, M., Maclean, I. M. D., Crowther, T. W., Bailey, J. J., Haesen, S., Klinges, D. H., Niittynen, P., Scheffers, B. R., Van Meerbeek, K., Aartsma, P., Abdalaze, O., Abedi, M., Aerts, R., Ahmadian, N., Ahrends, A., Alatalo, J. M., Alexander, J. M., Allonsius, C. N., Altman, J., Ammann, C., Andres, C., Andrews, C., Ardö, J., Arriga, N., Arzac, A., Aschero, V., Assis, R. L., Assmann, J. J., Bader, M. Y., Bahalkeh, K., Barančok, P., Barrio, I. C., Barros, A., Barthel, M., Basham, E. W., Bauters, M., Bazzichetto, M., Marchesini, L. B., Bell, M. C., Benavides, J. C., Benito Alonso, J. L., Berauer, B. J., Bjerke, J. W., Björk, R. G., Björkman, M. P., Björnsdóttir, K., Blonder, B., Boeckx, P., Boike, J., Bokhorst, S., Brum, B. N. S., Brůna, J., Buchmann, N., Buysse, P., Camargo, J. L., Campoe, O. C., Candan, O., Canessa, R., Cannone, N., Carbognani, M., Carnicer, J., Casanova-Katny, A., Cesarz, S., Chojnicki, B., Choler, P., Chown, S. L., Cifuentes, E. F., Čiliak, M., Contador, T., Convey, P., Cooper, E. J., Cremonese, E., Curasi, S. R., Curtis, R., Cutini, M., Dahlberg, C. J., Daskalova, G. N., De Pablo, M. A., Della Chiesa, S., Dengler, J., Deronde, B., Descombes, P., Di Cecco, V., Di Musciano, M., Dick, J., Dimarco, R. D., Dolezal, J., Dorrepaal, E., Dušek, J., Eisenhauer, N., Eklundh, L., Erickson, T. E., Erschbamer, B., Eugster, W., Ewers, R. M., Exton, D. A., Fanin, N., Fazlioglu, F., Feigenwinter, I., Fenu, G., Ferlian, O., Fernández Calzado, M. R., Fernández-Pascual, E., Finckh, M., Higgens, R. F., Forte, T. G. W., Freeman, E. C., Frei, E. R., Fuentes-Lillo, E., García, R. A., García, M. B., Géron, C., Gharun, M., Ghosn, D., Gigauri, K., Gobin, A., Goded, I., Goeckede, M., Gottschall, F., Goulding, K., Govaert, S., Graae, B. J., Greenwood, S., Greiser, C., Grelle, A., Guénard, B., Guglielmin, M., Guillemot, J., Haase, P., Haider, S., Halbritter, A. H., Hamid, M., Hammerle, A., Hampe, A., Haugum, S. V., Hederová, L., Heinesch, B., Helfter, C., Hepenstrick, D., Herberich, M., Herbst, M., Hermanutz, L., Hik, D. S., Hoffrén, R., Homeier, J., Hörtnagl, L., Høye, T. T., Hrbacek, F., Hylander, K., Iwata, H., Jackowicz-Korczynski, M. A., Jactel, H., Järveoja, J., Jastrzębowski, S., Jentsch, A., Jiménez, J. J., Jónsdóttir, I. S., Jucker, T., Jump, A. S., Juszczak, R., Kanka, R., Kašpar, V., Kazakis, G., Kelly, J., Khuroo, A. A., Klemedtsson, L., Klisz, M., Kljun, N., Knohl, A., Kobler, J., Kollár, J., Kotowska, M. M., Kovács, B., Kreyling, J., Lamprecht, A., Lang, S. I., Larson, C., Larson, K., Laska, K., Le Maire, G., Leihy, R. I., Lens, L., Liljebladh, B., Lohila, A., Lorite, J., Loubet, B., Lynn, J., Macek, M., Mackenzie, R., Magliulo, E., Maier, R., Malfasi, F., Máliš, F., Man, M., Manca, G., Manco, A., Manise, T., Manolaki, P., Marciniak, F., Matula, R., Mazzolari, A. C., Medinets, S., Medinets, V., Meeussen, C., Merinero, S., Mesquita, R. D. C. G., Meusburger, K., Meysman, F. J. R., Michaletz, S. T., Milbau, A., Moiseev, D., Moiseev, P., Mondoni, A., Monfries, R., Montagnani, L., Moriana-Armendariz, M., Morra Di Cella, U., Mörsdorf, M., Mosedale, J. R., Muffler, L., Muñoz-Rojas, M., Myers, J. A., Myers-Smith, I. H., Nagy, L., Nardino, M., Naujokaitis-Lewis, I., Newling, E., Nicklas, L., Niedrist, G., Niessner, A., Nilsson, M. B., Normand, S., Nosetto, M. D., Nouvellon, Y., Nuñez, M. A., Ogaya, R., Ogée, J., Okello, J., Olejnik, J., Olesen, J. E., Opedal, Ø. H., Orsenigo, S., Palaj, A., Pampuch, T., Panov, A. V., Pärtel, M., Pastor, A., Pauchard, A., Pauli, H., Pavelka, M., Pearse, W. D., Peichl, M., Pellissier, L., Penczykowski, R. M., Penuelas, J., Petit Bon, M., Petraglia, A., Phartyal, S. S., Phoenix, G. K., Pio, C., Pitacco, A., Pitteloud, C., Plichta, R., Porro, F., Portillo-Estrada, M., Poulenard, J., Poyatos, R., Prokushkin, A. S., Puchalka, R., Puşcaş, M., Radujković, D., Randall, K., Ratier Backes, A., Remmele, S., Remmers, W., Renault, D., Risch, A. C., Rixen, C., Robinson, S. A., Robroek, B. J. M., Rocha, A. V., Rossi, C., Rossi, G., Roupsard, O., Rubtsov, A. V., Saccone, P., Sagot, C., Sallo Bravo, J., Santos, C. C., Sarneel, J. M., Scharnweber, T., Schmeddes, J., Schmidt, M., Scholten, T., Schuchardt, M., Schwartz, N., Scott, T., Seeber, J., Segalin De Andrade, A. C., Seipel, T., Semenchuk, P., Senior, R. A., Serra-Diaz, J. M., Sewerniak, P., Shekhar, A., Sidenko, N. V., Siebicke, L., Siegwart Collier, L., Simpson, E., Siqueira, D. P., Sitková, Z., Six, J., Smiljanic, M., Smith, S. W., Smith-Tripp, S., Somers, B., Sørensen, M. V., Souza, J. J. L. L., Souza, B. I., Souza Dias,

A., Spasojevic, M. J., Speed, J. D. M., Spicher, F., Stanisci, A., Steinbauer, K., Steinbrecher, R., Steinwandter, M., Stemkovski, M., Stephan, J. G., Stiegler, C., Stoll, S., Svátek, M., Svoboda, M., Tagesson, T., Tanentzap, A. J., Tanneberger, F., Theurillat, J.-P., Thomas, H. J. D., Thomas, A. D., Tielbörger, K., Tomaselli, M., Treier, U. A., Trouillier, M., Turtureanu, P. D., Tutton, R., Tyystjärvi, V. A., Ueyama, M., Ujházy, K., Ujházyová, M., Uogintas, D., Urban, A. V., Urban, J., Urbaniak, M., Ursu, T.-M., Vaccari, F. P., Van De Vondel, S., Van Den Brink, L., Van Geel, M., Vandvik, V., Vangansbeke, P., Varlagin, A., Veen, G. F., Veenendaal, E., Venn, S. E., Verbeeck, H., Verbrugggen, E., Verheijen, F. G. A., Villar, L., Vitale, L., Vittoz, P., Vives-Ingla, M., Von Oppen, J., Walz, J., Wang, R., Wang, Y., Way, R. G., Wedegärtner, R. E. M., Weigel, R., Wild, J., Wilkinson, M., Wilmking, M., Wingate, L., Winkler, M., Wipf, S., Wohlfahrt, G., Xenakis, G., Yang, Y., Yu, Z., Yu, K., Zellweger, F., Zhang, J., Zhang, Z., Zhao, P., Ziemblińska, K., Zimmermann, R., Zong, S., Zyryanov, V. I., Nijs, I., and Lenoir, J.: Global Maps of Soil Temperature, Global Change Biology, 28, 3110–3144, https://doi.org/10.1111/gcb.16060, 2022.

Lemmetyinen, J., Kontu, A., Kärnä, J.-P., Vehviläinen, J., Takala, M., and Pulliainen, J.: Correcting for the Influence of Frozen Lakes in Satellite Microwave Radiometer Observations through Application of a Microwave Emission Model, Remote Sensing of Environment, 115, 3695–3706, https://doi.org/10.1016/j.rse.2011.09.008, 2011.

Lemmetyinen, J., Schwank, M., Rautiainen, K., Kontu, A., Parkkinen, T., Mätzler, C., Wiesmann, A., Wegmüller, U., Derksen, C., Toose, P., Roy, A., and Pulliainen, J.: Snow Density and Ground Permittivity Retrieved from L-band Radiometry: Application to Experimental Data, Remote Sensing of Environment, 180, 377–391, https://doi.org/10.1016/j.rse.2016.02.002, 2016.

Liebe, H. J., Hufford, G. A., and Manabe, T.: A Model for the Complex Permittivity of Water at Frequencies below 1 THz, International Journal of Infrared and Millimeter Waves, 12, 659–675, https://doi.org/10.1007/BF01008897, 1991.

Liston, G. E., Mcfadden, J. P., Sturm, M., and Pielke, R. A.: Modelled Changes in Arctic Tundra Snow, Energy and Moisture Fluxes Due to Increased Shrubs, Global Change Biology, 8, 17–32, https://doi.org/10.1046/j.1354-1013.2001.00416.x, 2002.

Macelloni, G., Brogioni, M., Leduc-Leballeur, M., Montomoli, F., Bartsch, A., Mialon, A., Ritz, C., Soteras, J. C., Stammer, D., Picard, G., De Carolis, G., Boutin, J., Johnson, J. T., Nicholls, K. W., Jezek, K., Rautiainen, K., Kaleschke, L., Bertino, L., Tsang, L., Van Den Broeke, M., Skou, N., and Tietsche, S.: Cryorad: A Low Frequency Wideband Radiometer Mission for the Study of the Cryosphere, in: IGARSS 2018 - 2018 IEEE International Geoscience and Remote Sensing Symposium, pp. 1998–2000, IEEE, Valencia, ISBN 978-1-5386-7150-4, https://doi.org/10.1109/IGARSS.2018.8519172, 2018.

Marchand, N., Royer, A., Krinner, G., Roy, A., Langlois, A., and Vargel, C.: Snow-Covered Soil Temperature Retrieval in Canadian Arctic Permafrost Areas, Using a Land Surface Scheme Informed with Satellite Remote Sensing Data, Remote Sensing, 10, 1703, https://doi.org/10.3390/rs10111703, 2018.

Mätzler, C., ed.: Thermal Microwave Radiation: Applications for Remote Sensing, no. 52 in IET Electromagnetic Waves Series, IET, London, ISBN 978-0-86341-573-9 978-1-84919-002-2, https://doi.org/10.1049/PBEW052E, 2006.

Mätzler, C. and Wiesmann, A.: Documentation for MEMLS, Version 3 'Microwave Emission Model of Layered Snowpacks', Tech. rep., Institute of Applied Physics (IAP) at the University of Bern., 2012.

Mavrovic, A., Sonnentag, O., Lemmetyinen, J., Voigt, C., Rutter, N., Mann, P., Sylvain, J.-D., and Roy, A.: Environmental Controls of Winter Soil Carbon Dioxide Fluxes in Boreal and Tundra Environments, Biogeosciences, 20, 5087–5108, https://doi.org/10.5194/bg-20-5087-2023, 2023.

Mialon, A., Royer, A., Fily, M., and Picard, G.: Daily Microwave-Derived Surface Temperature over Canada/Alaska, Journal of Applied Meteorology and Climatology, 46, 591–604, https://doi.org/10.1175/JAM2485.1, 2007.

Mialon, A., Coret, L., Kerr, Y., Secherre, F., and Wigneron, J.-P.: Flagging the Topographic Impact on the SMOS Signal, IEEE Transactions on Geoscience and Remote Sensing, 46, 689–694, https://doi.org/10.1109/TGRS.2007.914788, 2008.

Mialon, A., Rodríguez-Fernández, N. J., Santoro, M., Saatchi, S., Mermoz, S., Bousquet, E., and Kerr, Y. H.: Evaluation of the Sensitivity of SMOS L-VOD to Forest Above-Ground Biomass at Global Scale, Remote Sensing, 12, 1450, https://doi.org/10.3390/rs12091450, 2020.

Mironov, V., Kosolapova, L., and Fomin, S.: Physically and Mineralogically Based Spectroscopic Dielectric Model for Moist Soils, IEEE Transactions on Geoscience and Remote Sensing, 47, 2059–2070, https://doi.org/10.1109/TGRS.2008.2011631, 2009.

Mironov, V. L., Kosolapova, L. G., Savin, I. V., and Muzalevskiy, K. V.: Temperature Dependent Dielectric Model at 1.4 GHz for a Tundra Organic-Rich Soil Thawed and Frozen, in: 2015 IEEE International Geoscience and Remote Sensing Symposium (IGARSS), pp. 2016–2019, IEEE, Milan, Italy, ISBN 978-1-4799-7929-5, https://doi.org/10.1109/IGARSS.2015.7326194, 2015.

Murfitt, J., Duguay, C., Picard, G., and Gunn, G.: Forward Modelling of Synthetic Aperture Radar Backscatter from Lake Ice over Canadian Subarctic Lakes, Remote Sensing of Environment, 286, 113 424, https://doi.org/10.1016/j.rse.2022.113424, 2023.

Natali, S. M., Watts, J. D., Rogers, B. M., Potter, S., Ludwig, S. M., Selbmann, A.-K., Sullivan, P. F., Abbott, B. W., Arndt, K. A., Birch, L., Björkman, M. P., Bloom, A. A., Celis, G., Christensen, T. R., Christiansen, C. T., Commane, R., Cooper, E. J., Crill, P., Czimczik, C., Davydov, S., Du, J., Egan, J. E., Elberling, B., Euskirchen, E. S., Friborg, T., Genet, H., Göckede, M., Goodrich, J. P., Grogan, P., Helbig, M., Jafarov, E. E., Jastrow, J. D., Kalhori, A. A. M., Kim, Y., Kimball, J. S., Kutzbach, L., Lara, M. J., Larsen, K. S., Lee, B.-Y., Liu, Z., Loranty, M. M., Lund, M., Lupascu, M., Madani, N., Malhotra, A., Matamala, R., McFarland, J., McGuire, A. D., Michelsen, A., Minions, C., Oechel, W. C., Olefeldt, D., Parmentier, F.-J. W., Pirk, N., Poulter, B., Quinton, W., Rezanezhad, F., Risk, D., Sachs, T., Schaefer, K., Schmidt, N. M., Schuur, E. A. G., Semenchuk, P. R., Shaver, G., Sonnentag, O., Starr, G., Treat, C. C., Waldrop, M. P., Wang, Y., Welker, J., Wille, C., Xu, X., Zhang, Z., Zhuang, Q., and Zona, D.: Large Loss of CO2 in Winter Observed across the Northern Permafrost Region, Nature Climate Change, 9, 852–857, https://doi.org/10.1038/s41558-019-0592-8, 2019.

Oechel, W., Verfaillie, J., Vourlitis, G., and Zulueta, R.: CARVE: L1 In-situ Carbon and CH4 Flux and Meteorology at EC Towers, Alaska, 2011-2015, https://doi.org/10.3334/ORNLDAAC/1424, 2016.

Ortet, J., Mialon, A., Kerr, Y., Royer, A., Berg, A., Boike, J., Humphreys, E., Gibon, F., Richaume, P., Bircher-Adrot, S., Gorrab, A., and Roy, A.: Evaluating Soil Moisture Retrieval in Arctic and Sub-Arctic Environments Using Passive Microwave Satellite Data, International Journal of Digital Earth, 17, 2385 079, https://doi.org/10.1080/17538947.2024.2385079, 2024.

Oveisy, A., Boegman, L., and Imberger, J.: Three-dimensional Simulation of Lake and Ice Dynamics during Winter, Limnology and Oceanography, 57, 43–57, https://doi.org/10.4319/lo.2012.57.1.0043, 2012.

Pardo Lara, R., Berg, A. A., Warland, J., and Tetlock, E.: In Situ Estimates of Freezing/Melting Point Depression in Agricultural Soils Using Permittivity and Temperature Measurements, Water Resources Research, 56, e2019WR026 020, https://doi.org/10.1029/2019WR026020, 2020.

Park, C.-H., Behrendt, A., LeDrew, E., and Wulfmeyer, V.: New Approach for Calculating the Effective Dielectric Constant of the Moist Soil for Microwaves, Remote Sensing, 9, 732, https://doi.org/10.3390/rs9070732, 2017.

Park, C.-H., Montzka, C., Jagdhuber, T., Jonard, F., De Lannoy, G., Hong, J., Jackson, T. J., and Wulfmeyer, V.: A Dielectric Mixing Model Accounting for Soil Organic Matter, Vadose Zone Journal, 18, 190 036, https://doi.org/10.2136/vzj2019.04.0036, 2019.

Parrens, M., Wigneron, J.-P., Richaume, P., Al Bitar, A., Mialon, A., Fernandez-Moran, R., Al-Yaari, A., O'Neill, P., and Kerr, Y.: Considering Combined or Separated Roughness and Vegetation Effects in Soil Moisture Retrievals, International Journal of Applied Earth Observation and Geoinformation, 55, 73–86, https://doi.org/10.1016/j.jag.2016.11.001, 2017.

Poggio, L., De Sousa, L. M., Batjes, N. H., Heuvelink, G. B. M., Kempen, B., Ribeiro, E., and Rossiter, D.: SoilGrids 2.0: Producing Soil Information for the Globe with Quantified Spatial Uncertainty, SOIL, 7, 217–240, https://doi.org/10.5194/soil-7-217-2021, 2021.

Preethi, K., Li, X., Fernandez-Moran, R., Liu, X., Xing, Z., Frappart, F., Piles, M., Lanka, K., and Wigneron, J.-P.: A New Calibration of Soil Roughness Effects in the SMOS-IC Algorithm for Soil Moisture and VOD Retrievals, in: IGARSS 2024 - 2024 IEEE International Geoscience and Remote Sensing Symposium, pp. 6701–6704, IEEE, Athens, Greece, ISBN 9798350360325, https://doi.org/10.1109/IGARSS53475.2024.10642708, 2024.

Rautiainen, K., Lemmetyinen, J., Pulliainen, J., Vehvilainen, J., Drusch, M., Kontu, A., Kainulainen, J., and Seppanen, J.: L-Band Radiometer Observations of Soil Processes in Boreal and Subarctic Environments, IEEE Transactions on Geoscience and Remote Sensing, 50, 1483–1497, https://doi.org/10.1109/TGRS.2011.2167755, 2012.

Rautiainen, K., Lemmetyinen, J., Schwank, M., Kontu, A., Ménard, C. B., Mätzler, C., Drusch, M., Wiesmann, A., Ikonen, J., and Pulliainen, J.: Detection of Soil Freezing from L-band Passive Microwave Observations, Remote Sensing of Environment, 147, 206–218, https://doi.org/10.1016/j.rse.2014.03.007, 2014.

Rautiainen, K., Parkkinen, T., Lemmetyinen, J., Schwank, M., Wiesmann, A., Ikonen, J., Derksen, C., Davydov, S., Davydova, A., Boike, J., Langer, M., Drusch, M., and Pulliainen, J.: SMOS Prototype Algorithm for Detecting Autumn Soil Freezing, Remote Sensing of Environment, 180, 346–360, https://doi.org/10.1016/j.rse.2016.01.012, 2016.

Rouse, W. R., Douglas, M. S. V., Hecky, R. E., Hershey, A. E., Kling, G. W., Lesack, L., Marsh, P., Mcdonald, M., Nicholson, B. J., Roulet, N. T., and Smol, J. P.: EFFECTS OF CLIMATE CHANGE ON THE FRESHWATERS OF ARCTIC AND SUBARCTIC NORTH AMERICA, Hydrological Processes, 11, 873–902, https://doi.org/10.1002/(SICI)1099-1085(19970630)11:8<873::AID-HYP510>3.0.CO;2-6, 1997.

Roy, A., Royer, A., Derksen, C., Brucker, L., Langlois, A., Mialon, A., and Kerr, Y. H.: Evaluation of Spaceborne L-Band Radiometer Measurements for Terrestrial Freeze/Thaw Retrievals in Canada, IEEE Journal of Selected Topics in Applied Earth Observations and Remote Sensing, 8, 4442–4459, https://doi.org/10.1109/JSTARS.2015.2476358, 2015.

Roy, A., Toose, P., Williamson, M., Rowlandson, T., Derksen, C., Royer, A., Berg, A. A., Lemmetyinen, J., and Arnold, L.: Response of L-Band Brightness Temperatures to Freeze/Thaw and Snow Dynamics in a Prairie Environment from Ground-Based Radiometer Measurements, Remote Sensing of Environment, 191, 67–80, https://doi.org/10.1016/j.rse.2017.01.017, 2017.

Roy, A., Leduc-Leballeur, M., Picard, G., Royer, A., Toose, P., Derksen, C., Lemmetyinen, J., Berg, A., Rowlandson, T., and Schwank, M.: Modelling the L-Band Snow-Covered Surface Emission in a Winter Canadian Prairie Environment, Remote Sensing, 10, 1451, https://doi.org/10.3390/rs10091451, 2018.

Royer, A., Domine, F., Roy, A., Langlois, A., Marchand, N., and Davesne, G.: New Northern Snowpack Classification Linked to Vegetation Cover on a Latitudinal Mega-Transect across Northeastern Canada, Écoscience, 28, 225–242, https://doi.org/10.1080/11956860.2021.1898775, 2021a.

Royer, A., Picard, G., Vargel, C., Langlois, A., Gouttevin, I., and Dumont, M.: Improved Simulation of Arctic Circumpolar Land Area Snow Properties and Soil Temperatures, Frontiers in Earth Science, 9, 685 140, https://doi.org/10.3389/feart.2021.685140, 2021b.

Schaefer, G. L., Cosh, M. H., and Jackson, T. J.: The USDA Natural Resources Conservation Service Soil Climate Analysis Network (SCAN), Journal of Atmospheric and Oceanic Technology, 24, 2073–2077, https://doi.org/10.1175/2007JTECHA930.1, 2007.

Schmugge, T. J.: Remote Sensing of Soil Moisture: Recent Advances, IEEE Transactions on Geoscience and Remote Sensing, GE-21, 336–344, https://doi.org/10.1109/TGRS.1983.350563, 1983.

Schuur, E. A. G., McGuire, A. D., Schädel, C., Grosse, G., Harden, J. W., Hayes, D. J., Hugelius, G., Koven, C. D., Kuhry, P., Lawrence, D. M., Natali, S. M., Olefeldt, D., Romanovsky, V. E., Schaefer, K., Turetsky, M. R., Treat, C. C., and Vonk, J. E.: Climate Change and the Permafrost Carbon Feedback, Nature, 520, 171–179, https://doi.org/10.1038/nature14338, 2015.

Schwank, M., Stahli, M., Wydler, H., Leuenberger, J., Matzler, C., and Fluhler, H.: Microwave L-band Emission of Freezing Soil, IEEE Transactions on Geoscience and Remote Sensing, 42, 1252–1261, https://doi.org/10.1109/TGRS.2004.825592, 2004.

Schwank, M., Rautiainen, K., Mätzler, C., Stähli, M., Lemmetyinen, J., Pulliainen, J., Vehviläinen, J., Kontu, A., Ikonen, J., Ménard, C. B., Drusch, M., Wiesmann, A., and Wegmüller, U.: Model for Microwave Emission of a Snow-Covered Ground with Focus on L Band, Remote Sensing of Environment, 154, 180–191, https://doi.org/10.1016/j.rse.2014.08.029, 2014.

Schwank, M., Matzler, C., Wiesmann, A., Wegmuller, U., Pulliainen, J., Lemmetyinen, J., Rautiainen, K., Derksen, C., Toose, P., and Drusch, M.: Snow Density and Ground Permittivity Retrieved from L-Band Radiometry: A Synthetic Analysis, IEEE Journal of Selected Topics in Applied Earth Observations and Remote Sensing, 8, 3833–3845, https://doi.org/10.1109/JSTARS.2015.2422998, 2015.

Schwank, M., Kontu, A., Mialon, A., Naderpour, R., Houtz, D., Lemmetyinen, J., Rautiainen, K., Li, Q., Richaume, P., Kerr, Y., and Mätzler, C.: Temperature Effects on L-band Vegetation Optical Depth of a Boreal Forest, Remote Sensing of Environment, 263, 112 542, https://doi.org/10.1016/j.rse.2021.112542, 2021.

Shiklomanov, N. I.: Non-Climatic Factors and Long-Term, Continental-Scale Changes in Seasonally Frozen Ground, Environmental Research Letters, 7, 011 003, https://doi.org/10.1088/1748-9326/7/1/011003, 2012.

Turetsky, M. R., Abbott, B. W., Jones, M. C., Anthony, K. W., Olefeldt, D., Schuur, E. A. G., Grosse, G., Kuhry, P., Hugelius, G., Koven, C., Lawrence, D. M., Gibson, C., Sannel, A. B. K., and McGuire, A. D.: Carbon Release through Abrupt Permafrost Thaw, Nature Geoscience, 13, 138–143, https://doi.org/10.1038/s41561-019-0526-0, 2020.

Ulaby, F. and Long, D.: Microwave Radar and Radiometric Remote Sensing, University of Michigan Press, ISBN 978-0-472-11935-6, https://doi.org/10.3998/0472119356, 2014.

Ulaby, F., Allen, C., Eger, G., and Kanemasu, E.: Relating the Microwave Backscattering Coefficient to Leaf Area Index, Remote Sensing of Environment, 14, 113–133, https://doi.org/10.1016/0034-4257(84)90010-5, 1984.

Urban, F.: Data Release Associated with Data Series - DOI/GTN-P Climate and Active-Layer Data Acquired in the National Petroleum Reserve-Alaska and the Arctic National Wildlife Refuge, 1998-2019 (Ver. 3.0, March 2021), https://doi.org/10.5066/F7VX0FGB, 2017.

Wang, J. R. and Choudhury, B. J.: Remote Sensing of Soil Moisture Content, over Bare Field at 1.4 GHz Frequency, Journal of Geophysical Research, 86, 5277, https://doi.org/10.1029/JC086iC06p05277, 1981.

Wang, Z., Kim, Y., Seo, H., Um, M.-J., and Mao, J.: Permafrost Response to Vegetation Greenness Variation in the Arctic Tundra through Positive Feedback in Surface Air Temperature and Snow Cover, Environmental Research Letters, 14, 044 024, https://doi.org/10.1088/1748-9326/ab0839, 2019.

Westermann, S., Langer, M., and Boike, J.: Systematic Bias of Average Winter-Time Land Surface Temperatures Inferred from MODIS at a Site on Svalbard, Norway, Remote Sensing of Environment, 118, 162–167, https://doi.org/10.1016/j.rse.2011.10.025, 2012.

Westermann, S., Østby, T. I., Gisnås, K., Schuler, T. V., and Etzelmüller, B.: A Ground Temperature Map of the North Atlantic Permafrost Region Based on Remote Sensing and Reanalysis Data, The Cryosphere, 9, 1303–1319, https://doi.org/10.5194/tc-9-1303-2015, 2015.

Wiesmann, A. and Mätzler, C.: Microwave Emission Model of Layered Snowpacks, Remote Sensing of Environment, 70, 307–316, https://doi.org/10.1016/S0034-4257(99)00046-2, 1999.

Wigneron, J.-P., Chanzy, A., Kerr, Y. H., Lawrence, H., Shi, J., Escorihuela, M. J., Mironov, V., Mialon, A., Demontoux, F., De Rosnay, P., and Saleh-Contell, K.: Evaluating an Improved Parameterization of the Soil Emission in L-MEB, IEEE Transactions on Geoscience and Remote Sensing, 49, 1177–1189, https://doi.org/10.1109/TGRS.2010.2075935, 2011.

Zhang, L., Zhao, T., Jiang, L., and Zhao, S.: Estimate of Phase Transition Water Content in Freeze–Thaw Process Using Microwave Radiometer, IEEE Transactions on Geoscience and Remote Sensing, 48, 4248–4255, https://doi.org/10.1109/TGRS.2010.2051158, 2010.

Zhang, T.: Influence of the Seasonal Snow Cover on the Ground Thermal Regime: An Overview, Reviews of Geophysics, 43, 2004RG000 157, https://doi.org/10.1029/2004RG000157, 2005.